Chiral perovskite optoelectronics

Guankui Long[1,8], Randy Sabatini[2,8], Makhsud I. Saidaminov[3,4,8], Girish Lakhwani[2], Abdullah Rasmita[1], Xiaogang Liu[5], Edward H. Sargent[3]*, Weibo Gao[1,6,7]*

[1]Division of Physics and Applied Physics, School of Physical and Mathematical Sciences, Nanyang Technological University, Singapore 637371, Singapore
[2]ARC Centre of Excellence in Exciton Science, School of Chemistry, University of Sydney, NSW 2006, Australia
[3]Department of Electrical and Computer Engineering, University of Toronto, 10 King's College Road, Toronto, Ontario M5S 3G4, Canada
[4]Department of Chemistry and Electrical & Computer Engineering, Centre for Advanced Materials and Related Technologies (CAMTEC), University of Victoria, 3800 Finnerty Rd, Victoria, BC V8P 5C2, Canada
[5]Department of Chemistry, National University of Singapore, 3 Science Drive 3, Singapore 117543, Singapore
[6]MajuLab, CNRS-Université de Nice-NUS-NTU International Joint Research Unit UMI 3654, Singapore
[7]The Photonics Institute and Centre for Disruptive Photonic Technologies, Nanyang Technological University, Singapore 637371, Singapore
[8]These authors contributed equally: Guankui Long, Randy Sabatini, Makhsud I. Saidaminov

*Correspondence to: ted.sargent@utoronto.ca; wbgao@ntu.edu.sg

Hybrid organic–inorganic perovskites (HOIPs) offer long carrier diffusion lengths, high absorption coefficients, tunable bandgaps and long spin lifetimes. The flexible crystal structure and ionic nature of HOIPs makes it possible to allow tune their material properties through rational design, including the incorporation of chiral organic ligands. Recently, chiral HOIPs have emerged as promising materials for chiroptoelectronics, spintronics and ferroelectricity. They exhibit high photoluminescence polarization (17% without an external magnetic field), good device performance (a circularly polarized photodetector had 100 times higher responsivity than one based on chiral metasurface) and high saturated polarization (~2 times higher than that of barium titanate). Here we review the latest advances in chiral HOIPs and investigate the specific benefits of combining chiral organic and inorganic components in perovskites. We discuss demonstrations of chiroptical and ferroelectric applications, and conclude with our perspective on the future opportunities for chiral HOIPs.

[H1] Introduction

In the past decade, hybrid organic–inorganic perovskites (HOIPs) have become an important materials family for optoelectronics. Low trap densities[1] and long carrier diffusions lengths[2-5] have led to solar cells with efficiency above 20%[6-9]; near-unity photoluminescence quantum yields and tunable emission have enabled high-performing light-emitting diodes (LEDs) spanning the visible and portions of the near infrared spectra[10-12]; and large optical gain has allowed low thresholds in both pulsed and continuous wave optically pumped lasing[13-17]. With high mobilities[18-21] and dielectric constants[22], these materials have also been explored as photodetectors[23,24]. In addition, their large Rashba splitting[25,26] and long spin lifetimes[27-29] have motivated research into spintronic applications[30-32].

HOIPs possess a flexible crystal structure and a tunable hybrid organic–inorganic composition. This enables the incorporation of chiral ligands[33-37], which allow perovskites to be used in chiroptoelectronic[38,39], ferroelectric[40-42] and chiro-spintronic[43,44] applications.

[H2] Chirality and its extension to perovskites

A material is chiral if its mirror image cannot be brought to coincide with it[45]. Chirality is found in the L-configuration of the natural α-amino acids except glycine and in the D-configuration of the saccharides and saccharide units in cellulose, starch and DNA. In addition, chiral templates and sites play an important role in biological recognition and assembly. The community has harnessed this property, for example in chiral catalysts that are widely employed in asymmetric synthesis of pharmaceuticals.

Based on non-centrosymmetric structures, chiral materials can exhibit optical rotation[46], circular dichroism[47], second-harmonic generation (SHG)[48],

piezoelectricity[40], pyroelectricity[49], ferroelectricity[50] and topological quantum properties[51]. Thus, chiral materials have potential for application in chiroptoelectronics, including in circularly polarized light (CPL) photodetectors[52-55], circularly polarized LEDs[56-60], bioresponsive imaging[61-63], 3D displays[64,65], as well as applications in quantum computing[66,67], quantum communication[68-70], non-volatile memory devices[71] and spintronics[30,43,44,72] (Fig. 1).

Chiroptical effects can be reproduced by incorporating metasurfaces and optical elements (such as quarter-wave plates); however, some applications require chiral materials. Optical elements decrease efficiency, and metasurfaces increase the complexity, and often cost, of a system. Chiral materials offer an advantage in applications requiring small footprints and ease of fabrication. In many of the applications listed above (such as on-chip circularly polarized photodetectors[52-55], LEDs[73,74] and polarization-based memory storage[75,76]), additional elements hinder fabrication and performance, thus true chiral materials are required.

The first demonstration of chirality in HOIPs was a 1D chiral perovskite single crystal in 2003[33], with 2D chiral perovskite single crystals following in 2006 (FIG. 2)[34]. However, their chiroptical properties were not explored initially. Only after breakthroughs in power conversion efficiency of perovskite solar cells[77,78] investigation began into many aspects of their optical properties[14-16]. Chiral perovskites reemerged in 2017, when the first chiroptical study was performed[47]. Since then, additional chiral HOIPs have been reported, including chiral perovskite nanocrystals[79,80], cogels[81], nanoplatelets[82] and low-dimensional chiral perovskites[83]. Whereas metal-free 3D chiral perovskites have been synthesized[84], metal-containing 3D chiral HOIPs have yet to be demonstrated, although they have been theoretically predicted to be both thermodynamically and kinetically stable[85].

Chiral perovskites are classified into 65 different space groups, known as the Sohncke space groups[91], and exhibit chiroptical and ferroelectric properties according to the Neumann–Curie principle[92,93] (FIG. 3). In Box 1, we define key terms that are used throughout this Review to discuss chiroptical and ferroelectric properties of chiral perovskites (see also Section 1 of the Supplementary Information for a more detailed description).

The optical and electronic properties of chiral perovskites have been recently reviewed[86]; in the present Review, we focus on their structure–property relationships. We also discuss the motivation for incorporating chiral HOIPs, and cover chiroptical effects[46,87] and ferroelectricity[50,88], as well as the concepts underlying chiral induction (that is, chirality transfer)[89,90]. We then review applications such as circularly polarized photo-detection[38], spin manipulation[39,83], high-order nonlinear chiroptical effects[48,80] and ferroelectricity[40,41]. We close with a forward-looking perspective on chiral HOIPs.

[H1] Design of chiral perovskites

When a perovskite material incorporates chiral organic molecules, they can impart their chiral properties to it[89]. This chirality transfer can be mediated through the formation of chemical bonds or even through spatial interactions between a chiral and an achiral system[89,90]. Table 1 summarizes the different chirality transfer mechanisms in chiral HOIPs[47,82,96]. They include: ligand-induced chiral inorganic structure (I, such as in chiral perovskite single crystals[33,34]); chiral distortion of the inorganic surface (II, such as in chiral perovskite nanocrystals[79,80]); chiral patterning of the surface ligands[101,102] (III); and electronic coupling between the chiral organic molecules and the inorganic structure (IV, chiral field effect)[103,104].

[H2] Chirality through chiral ligands

[H3] Direct synthesis

Chiral perovskites can be synthesized directly using chiral ligands to introduce chirality (FIG. 4a), enabling 0D, 1D, 2D, quasi-2D and 3D chiral HOIPs[33,34,83]. Low-dimensional HOIPs contain a greater percentage of chiral organic ligands and thus should exhibit a higher degree of chirality. For example, decreasing values of the anisotropy factor g_{abs} were observed for quasi-2D perovskites as the value of <n> (the number of inorganic layers between the chiral organic ligands) increased[83]. To date, only a select group of chiral ligands has been employed with perovskites (FIG. 4a).

The first chiral HOIP, incorporating the enantiomeric ligand (*S*)-methylbenzylammonium (*S*-MBA, FIG. 4a) was reported in 2003[33], and the corresponding 2D chiral HOIP single crystal in 2006[34]. Structurally, *R*(or *S*)-MBAPbX_3, (X=Cl, Br or I) exhibits 1D polymeric face-sharing structures, whereas (*R*(or *S*)-MBA)$_2PbI_4$ exhibits 2D corner-sharing layered structures (FIG. 4b)[34]. These enantiomers exhibit essentially the same cell parameters with mirror configuration and belong to the same Sohncke space group of $P2_12_12_1$. Chiral HOIPs were then extended to a new chiral ligand, 1-cyclohexylethylammonium (CHEA, FIG. 4a)[105].

A series of 1D chiral HOIPs emitting white light were reported; the emission was attributed to exciton self-trapping owing to the quantum confinement in low-dimensional perovskites[35,106-108]. As a result of introducing *R*-3-ammoniopiperidin-1-ium (3APD, FIG. 4a) as the chiral source, (*R*-3APD)$PbCl_4 \cdot H_2O$ exhibits tunable emission from blue to yellow under different excitation wavelengths, with a high color rendering index of 93.9[35]. Another chloride-based chiral HOIP with *R* or *S*-1-(1-naphthyl)ethylammonium (NEA) as the chiral ligand (FIG. 4a) was reported[109]; the resulting (*R*-NEA)$_2Pb_4Cl_{10}$·2DMF and (*S*-NEA)$_2Pb_4Cl_{10}$·2DMF exhibit a 2D layered structure (DMF: *N*,*N*-dimethylformamide), and both enantiomers belong to the $P2_1$

Sohncke space group. Interestingly, coordination four, five and six were observed for Pb (II) atoms in these 2D chiral HOIPs[109]. Other 2D chiral hybrid organic-inorganic lead perovskites based on MPEA[48] (*β*-methylphenethylammonium, FIG. 4a) and CMBA[40] (1-(4-chlorophenyl)ethylammonium, FIG. 4a), were also reported recently; we discuss them in the sections on nonlinear chiroptical applications and on ferroelectrics.

Lead-free chiral HOIPs based on tin[110,111], bismuth[37], copper[112-114], manganese[41], cadmium[115] and cobalt[116], were also reported, yet their chiroptoelectronic and chiro-spintronic properties have not been studied yet.

[H3] Post-synthetic chiral ligand exchange

In post-synthetic chiral ligand exchange[117], the original ligands are exchanged partially or fully with chiral ligands. Unlike direct synthesis, in which chiral ligands influence the crystal structure, the chirality in this case is due to chiral surface distortion of the nanocrystals (induced by the capped ligands), chiral patterning of the surface ligands, or the chiral field effect[47,82,96].

Chiral perovskite nanocrystals (*R*-DACH-NCs and *S*-DACH-NCs) were obtained by replacing the oleylamine ligands with a small amount of chiral (1*R*, 2*R*)-1,2-diaminocyclohexane (*R*-DACH) or (1*S*, 2*S*)-1,2-diaminocyclohexane (*S*-DACH) ligands (FIG. 5a)[79]. These chiral nanocrystals exhibit no circular dichroism signal from the region of the first excitonic transition band of the nanocrystal core (~580 nm). However, they do exhibit circular dichroism from 240 nm to 540 nm owing to their chiral surface distortion and electronic interactions with the DACH ligands[79]. The

photoluminescence of the perovskite nanocrystals is completely quenched by the chiral ligands.

[H3] Chiral-ligand-assisted re-precipitation method

In chiral-ligand-assisted re-precipitation (CLARP), the ligands imprint chirality onto the electronic states of the quantum-confined perovskite. For instance, chirality was achieved in $CH_3NH_3PbBr_3$ perovskite nanoplatelets via CLARP using *R*- (or *S*-)MBA at room temperature[82]. The resulting circular dichroism spectra feature two regions: one arising from excitonic transitions of the perovskite (400–450 nm), the other from charge transfer transitions between the ligands and the nanoplatelets[82].

[H3] Chiral-ligand-assisted tip sonication method

Recently, a simple, scalable, single-step and polar-solvent-free method to synthesize high-quality perovskite nanocrystals was developed: direct tip sonication[119]. Through the replacement of the achiral organic capping ligands (on the surface of the nanocrystal) with chiral molecules, chiral perovskite nanocrystals could also be obtained. For example, *R*(or *S*-)-*α*-octylamine (FIG. 4a) was employed as the chiral ligand[80]. In this case, the chirality of the perovskite nanocrystals originates from the surface distortion induced by the chiral ligands (FIG. 5b).

[H2] Chirality through environment

Chirality can also be induced in achiral molecular systems by tuning the environmental conditions by using chiral solvents[120], external stimuli (such as strain[121]), self-assembly on chiral templated structures like DNA[122], a chiral bias inducing chiral amplification into a supramolecular helical structure[123], and photo-induced inversion of helical chirality[124].

Whereas chiral molecules are recognized via their stereogenic centers, helical structures possess a chirality axis about which molecules are spatially arranged to yield

non-superimposable mirror images[125]. 1D *M* and *P* chiral descriptors characterize left-handed and right-handed helices.

[H3] Helical chirality

A series of helical 1D chiral perovskites were synthesized through the introduction of achiral Schiff base cations, (*E*)-1-((3-Rbenzylidene)amino)pyridin-1-ium (*m*-RBz-1-APy$^+$; R=NO_2, Br, Cl, or F, FIG. 5c)[118]. Two types of highly polarized 1D $[PbI_3]_\infty$ chains are coupled to the achiral organic cations by Coulomb and van der Waals forces, and the organic cations adopt a kagome-like tubular architecture (FIG. 5d). The obtained crystals are all in the same Sohncke space group of $P6_3$ (point group: C_6), enabling ferroelectricity[92,93]. A dielectric hysteresis loop was observed in these chiral perovskites, with a saturated polarization of 48 μC/cm^2 at room temperature[118].

Another series of helical chiral perovskites were reported by using disulfide $H_3N(CH_2)_2SS(CH_2)_2NH_3$ ligands (a vital unit in biosystems) through solvothermal reaction[36]. The obtained α-$[H_3N(CH_2)_2SS(CH_2)_2NH_3PbI_5]\cdot H_3O$ crystalizes into the $P2_1$ Sohncke space group, which displays an *M* helicity (left-handed helical form), opposite to that of the right-handed helical DNA. When α-$[H_3N(CH_2)_2SS(CH_2)_2NH_3PbI_5]\cdot H_3O$ is heated to 75 °C, a phase transition (conformation change) occurs from helical α-phase to the achiral racemic β-phase[36].

[H3] Supramolecular chiral induction approach

When an achiral perovskite is incorporated into a chiral cogel, this induces chirality into the perovskite, as the achiral perovskite nanocrystals follow the chirality of the gel structure to produce a chiral packing through supramolecular co-assembly. Chiral perovskite cogels were formed by dispersing perovskite nanocrystals into chiral lipid *N*,*N*′-bis(octadecyl)-L-glutamic diamide (LGAm) or its enantiomer *N*,*N*′-

bis(octadecyl)-D-glutamic diamide (DGAm, FIG. 5e)[81]. Owing to the strong scattering from the gels, no obvious circular dichroism signal was observed in the gel states; however, different handedness of induced circularly polarized photoluminescence was observed in the chiral cogels. The degree of photoluminescence polarization reached 0.365% at room temperature for $CsPbBr_3$ nanocrystals in DGAm, comparable to the value of 0.33% for $CsPbBr_3$ nanocrystals in LGAm. The circularly polarized photoluminescence (CPPL) could only be observed in the assembled state and disappeared in the disassembled state, which could be obtained through heating or using a polar solvent such as chlorobenzene (FIG. 5e)[81].

[H2] Areas for improvement

For successful applications, the design of chiral perovskites must continue to advance. As discussed above, chirality has been introduced into perovskites via different strategies, each with their own advantages and disadvantages. Owing to their periodic nature, chiral perovskite single crystals exhibit stronger chirality than polycrystals and thin films. Thus, future studies will benefit from improving film quality.

Helical chiral perovskites can be obtained starting from achiral ligands[36,118]; however, their prediction and design are difficult. Symmetry analysis reveals that reported chiral perovskite single crystals have only a 2-fold rotation or 2-fold screw axis[33-37]. It is expected that structures incorporating higher-order symmetry operations will have stronger chirality. Theoretical modeling will aid in this effort.

Chiral perovskite nanocrystals offer solution stability with colloidal states. Unfortunately, although different approaches have been employed to synthesize them, their chirality is generally low. Incorporation of a chiral matrix could be an effective strategy to overcome this issue. In principle, if the absorption and emission of

perovskite nanocrystals overlap with the circularly polarized absorption (or transmittance) of the chiral matrix, stronger circularly polarized absorption and emission can be expected[126].

[H1] Chiroptoelectronic and ferroelectric applications

The chiroptical behavior of 2D chiral (R-MBA)$_2$PbI$_4$ and (S-MBA)$_2$PbI$_4$ films has been explored in 2017[47]. Strong circularly polarized transitions flank the excitonic peak, showing that chiral perovskites exhibit the Cotton effect (BOX 1)[127]. Circular differential scattering was also observed in the circular dichroism as the film thickness was increased[47]. However, when (R-MBA)$_2$PbI$_4$ or (S-MBA)$_2$PbI$_4$ powder was mixed with KBr to form a pellet, no obvious circular dichroism peaks were observed; this indicates that crystal orientation and crystallinity play a vital role in the total chirality of amorphous and polycrystalline chiral perovskite samples[47].

[H2] Circularly polarized photodetectors

Left-handed and right-handed circularly polarized light can be used as two independent channels to transmit information, doubling the rate of data transport compared to unpolarized light[128]. The development of CPL-based communication requires high-performance circularly polarized photodetectors and circularly polarized light sources. Unlike indirect methods of detecting and emitting circularly polarized light, chiral materials do not require additional optics, thus circularly polarized photodetectors and light sources based on chiral materials are promising for integrated and flexible devices.

HOIPs have been demonstrated as effective photodetectors owing to their low trap density[1], strong light sensitivity[23,24] and tunable absorptions[14]. Similarly, by combining the impressive optical and electrical properties of HOIPs with chirality, chiral HOIPs

should be promising for the detection of circularly polarized light[38,39]. Currently, there are only a few reports on direct circularly polarized light detection from different material systems[52-55]. A major challenge for CPL photodetectors is combining chirality (usually associated with organic molecules) and efficient charge transport (usually associated with inorganic semiconductors). Therefore, chiral HOIPs are especially promising, as they benefit from both aspects[38,39].

Recently, a CPL photodetector based on 1D chiral perovskites was reported (FIG. 6a)[38]. 1D chiral perovskites have the largest molar ratio of chiral ligands compared with 2D and quasi-2D chiral perovskites, and thus should exhibit the strongest CPL response. A relationship between the thickness of the chiral medium and its ability to distinguish left-handed circularly polarized (LCP) and right-handed circularly polarized (RCP) light ($\Delta c/c$) for photoconductive CPL detection was formulated as

$$\frac{\Delta c}{c} = \frac{c_L - c_R}{(c_L + c_R)/2} \approx \frac{\Delta\alpha \cdot d}{exp(\alpha_L d) - 1} \qquad \textbf{(1)}$$

where Δc is the difference between the carrier concentration generated by LCP and RCP light illumination ($\Delta c = c_L - c_R$), whereas c is the average carrier concentration ($c = (c_L + c_R)/2$). $\Delta\alpha$ is the difference between the absorption coefficients for LCP (α_L) and RCP light (α_R), and d is the thickness of the chiral medium. Increasing the thickness of the chiral medium results in a decrease of the CPL response (FIG. 6b). Thus, an optimal thickness of the chiral HOIPs film is necessary to achieve the most efficient CPL photo-detection.

At a low CPL intensity of 5 μW/cm^2 (395 nm), the responsivity reaches 120 mA/W (FIG. 6c), which is almost two orders of magnitude larger than the CPL photodetectors based on plasmonic silver metamaterials[53]. The distinguishability (g_{res}) of these chiral perovskite-based circularly polarized photodetectors is calculated as

$$g_{res} = \frac{2(R_L - R_R)}{R_L + R_R} \qquad \textbf{(2)}$$

where R_L and R_R are the responsivities of the circularly polarized photodetector under LCP and RCP light illumination, respectively. Similar to g_{abs}, g_{res} also ranges from -2 to 2, which stand for pure LCP or RCP light detection, whereas 0 indicates no distinguishability between LCP and RCP light. In the system we are discussing, the calculated g_{res} is 0.10 at 395 nm, higher than the anisotropy factor of 0.02 obtained from circular dichroism measurements (FIG. 6c); this discrepancy was attributed to the spin-dependent carrier generation[27], transport and collection[129] for chiral perovskites under CPL excitation. The performance of these 1D chiral perovskite-based CPL photodetectors remained almost the same after one month under ambient conditions without encapsulation. A flexible CPL photodetector was also fabricated on a polyethylene terephthalate substrate, and the performance exhibited negligible degradation upon 100 cycles of bending[38].

A CPL photodetector based on 2D chiral perovskite/MoS_2 heterojunctions was also reported[39]. The device reached a responsivity of 450 mA/W at 519 nm, and a detectivity of 2.2×10^{11} Jones[39]. The calculated g_{res} was 0.09 at 510 nm (FIG. 6d), similar to that of CPL photodetectors based on 1D chiral perovskites.

At this stage, the performance of CPL photodetectors is still far from that required for practical applications. In-depth work is still needed to increase the anisotropy factor (g_{abs}) of chiral perovskite materials (see Section 2 of the Supplementary Information). As outlined earlier, different strategies (such as better crystallinity, higher-order rotation/screw symmetry, chiral perovskites in chiral matrices) may prove effective to this end.

[H2] Circularly polarized light sources

In addition to data transfer, circularly polarized light sources have applications in bioresponsive imaging[61,62], 3D displays[64,65], anti-counterfeiting[130], quantum computing[66,67] and spintronics[43,44]. For example, light polarization is very important for high-contrast and efficient displays. To eliminate the glare from external light sources (such as sunlight), circularly polarized antiglare filters are used widely to trap ambient light in the display. However, if the light source is unpolarized, roughly half of the emitted light is blocked by the antiglare filters, substantially decreasing its brightness and efficiency. Chiral materials are promising because they produce circularly polarized light that can be transmitted unimpeded through the filters[54,60,131]. Recently, circularly polarized LEDs with degrees of electroluminescence polarization over 50% were reported[73,74].

HOIPs have been demonstrated as efficient LEDs, with external quantum efficiencies reaching over 20%[12,132,133]. Therefore, chiral HOIPs are promising candidates for circularly polarized light sources. However, 2D chiral perovskite films generally exhibit poor photoluminescence quantum yields (PLQYs) at room temperature, owing to strong non-radiative recombination[134]. To overcome this issue, low-dimensional chiral perovskites were developed (LDCPs, FIG. 7a). Through combined strategies of energy funneling[10,11] and chirality transfer[89,90], efficient emission was enabled while maintaining the intrinsic optical, electrical and spintronic properties of the perovskites[83]. Both circular dichroism and CPPL were observed in these LDCPs. They exhibited a PLQY of 90% due to strong energy funneling, and a 3% circularly polarized photoluminescence was observed in the absence of an external magnetic field (FIG. 7b–7d)[83]. For comparsion, 3D achiral perovskites can only achieve

a comparable degree of photoluminescence polarization under an external magnetic field of 5 T[135].

The photoluminescence polarization of LDCPs arises from asymmetric emission rates of LCP and RCP light based on Einstein coefficients[136]. In two level system, Einstein coefficients relate the absorption rate to the emission rate. Since the emission of LDCPs only originates from one excited state (the higher <n>) to the ground state, the system is effectively a two-level system. Hence, an asymmetric absorption rate (circular dichroism) between spin up and down implies asymmetric emission rate between the two-spin species. The degree of photoluminescence polarization can be tuned further through the Zeeman interaction by applying an external magnetic field. For *R*-LDCP, when a positive magnetic field is applied, the contribution by the intrinsic asymmetric emission rates and Zeeman interaction are synergystic. Therefore, the photoluminescence polarization increases when applying a positive magnetic field (FIG. 7c, range I). However, when a negative magnetic field is applied, there is a competition between the intrinsic asymmetric emission rates and the Zeeman interaction (FIG. 7c, range II and III). The photoluminescence polarization decreases to zero when the negative magnetic field reaches -2.8 T, where the contribution by intrinsic asymmetric emission rates balances the Zeeman splitting. Further increasing the negative magnetic field allows the Zeeman interaction to play the leading role, and the photoluminescence polarization becomes negative (FIG. 7c, range III)[83]. The magnetic field dependence results for these chiral perovskites (FIG. 7b,7c,7d) are fitted as

$$DP = \frac{g_{eff}\mu_B B}{k_B T} + DP_0 \qquad \textbf{(3)}$$

where g_{eff} is the effective g factor of the spin-1/2 electron and hole in the spin-pair species, μ_B is the Bohr magneton, B is the applied magnetic field, DP_0 is the degree of polarization introduced by the chirality in the absence of the magnetic field, k_B is the Boltzmann constant and T is the temperature. Based on the fitting results, the g_{eff} for the *R*-, *S*- and *rac*-LDCPs are 0.032, 0.031 and 0.027, respectively.

The influence of temperature on the photoluminescence polarization of pure 2D chiral $(R\text{-MBA})_2PbI_4$ and $(S\text{-MBA})_2PbI_4$ microplates has also been systematically investigated[39]. A record photoluminescence polarization of 17.3% was observed at 77 K[39]. With increasing temperature, the degree of photoluminescence polarization decreases substantially due to the enhanced electron–phonon couplings and thermal expansion interactions, which reduce the lattice distortion and thus decrease the chirality[39]. In addition, increased temperature also results in spin mixing, which further decreases the degree of polarization[135].

At this stage, most studies on CPL sources with chiral HOIPs have been performed at cryogenic temperatures. For practical application, future work should focus on achieving high photoluminescence polarization at elevated temperatures. This will require developing novel chiral perovskite materials with strong chirality[39], as *DP* has been shown to decrease dramatically with increasing temperatures[135]. A better understanding of this correlation may also help to direct synthesis toward weakening or even eliminating this temperature dependence.

[H2] Nonlinear chiroptical effects

Nonlinear optics describes a large body of phenomena in which a medium behaves nonlinearly with respect to optical excitations (in term of optical power). The magnitude of the nonlinearity gives a measure of medium-assisted light–light

interaction in the material. A strong nonlinear response is desirable in applications such as data processing, which use integrated photonic circuits for realizing higher data transmission rates[137], or nonlinear microscopy, in which nonlinearity helps to obtain more information on the studied sample[138]. Nonlinear effects can be classified by their order, or the number of interacting photons needed to describe the phenomena (for example, second-order nonlinear optics involve two-photon interactions). As a basic rule, the interaction becomes weaker as its order increases. Hence, the strongest nonlinear effects should be second order.

However, for even-order nonlinear optical responses like SHG, strict structural non-centrosymmetry is required[94]. A series of non-centrosymmetric achiral perovskites was reported recently, and SHG[139], two-photon absorption[140] and linear electro-optic effects[141] were observed. However, predicting or designing non-centrosymmetric achiral perovskites is challenging. Thus, the exploration of optical nonlinearities in perovskites has been focused mainly on the odd-order nonlinear optical effects[142,143]. Chiral HOIPs are intrinsically non-centrosymmetric and thus are promising for nonlinear chiroptical applications[48,80]. Additionally, because chiral HOIPs can couple to circularly polarized light, they can be utilized in chiral integrated photonic circuits[144-146], which have been shown to have higher efficiency than conventional circuits[147].

Nonlinear chiroptical effects were recently observed in 2D chiral HOIPs based on *β*-MPEA (FIG. 4a). A solvent-engineered chiral perovskite (FIG. 7e) was obtained by using an anti-solvent vapor-assisted crystallization strategy, in which dimethyl sulfoxide (DMSO) molecules axially coordinate with Pb^{2+} in the partially edge-shared octahedra in $(MPEA)_{1.5}PbBr_{3.5}(DMSO)_{0.5}$[48]. Both circular dichroism and polarization-dependent SHG were observed in these chiral perovskite nanowires.

Polarization-dependent SHG was observed under a circularly polarized excitation at 850 nm (FIG. 7f). The SHG circular dichroism (SHG-CD) is defined as:

$$\text{SHG-CD}=(I_{RCP} - I_{LCP})/(I_{RCP} + I_{LCP}) \quad \textbf{(4)}$$

where I_{RCP} and I_{LCP} are the SHG intensity under right-handed and left-handed circularly polarized excitation, respectively. Vertical and horizontal analyzers is used to analyze the polarization of the generated SHG signal. If the SHG is only due to the circular dichroism, the SHG intensity will be the same for both vertical and horizontal analyzer. In $(R\text{-MPEA})_{1.5}PbBr_{3.5}(DMSO)_{0.5}$ nanowires, the SHG-CD reaches 61.9% and 74.0% under vertical (yellow line) and horizontal analyzers (green line), respectively[48]. This indicates that chiral perovskites exhibit very large SHG-CD, and the slight difference may originate from the linear polarization contribution due to the nanowire structure.

Beyond second-order nonlinear effects, one important nonlinear chiroptical effect is two-photon absorption-based upconverted circularly polarized photoluminescence (TP-UCPPL), which has recently been observed in chiral perovskite nanocrystals[80]. Unlike traditional one-photon absorption CPPL, TP-UCPPL doubles the excitation wavelength. The CPPL of chiral perovskite nanocrystals in a poly(methyl methacrylate) (PMMA) matrix was measured, and the results indicated that two-photon and one-photon circularly-polarized excitations give a similar degree of photoluminescence polarization, around 0.25%[80]. Therefore, TP-UCPPL can replace one-photon absorption CPPL if the doubled wavelength is more suited for a specific application. Such applications include imaging of biosystems (where red or near-infrared light is needed to penetrate the skin)[148,149] and chiroptoelectronics (as telecommunications use near-infrared bands)[128].

Future work on nonlinear chiroptical effects should focus on determining the correlation between space group and efficiency in SHG and TP-UCPPL. Because non-

centrosymmetry is required, it will be important to learn which space group provides the strongest nonlinear chiroptical effects. From there, a more directed approach will be available to improve performance. Furthermore, the optimization of the phase-matching condition (between the SHG signal and excitation signal), working temperature and dimensionality will be important for SHG. The phase matching condition has a pronounced effect on the generated second harmonic power[150]. Likewise, temperature and dimensionality can affect the value of the second-order susceptibility[144]. Hence, optimization of all these parameters is necessary for practical application of second-order nonlinear chiroptics.

[H2] Ferroelectric properties

Ferroelectric materials are a class of functional materials that are widely used in electrocaloric devices, ferroelectric random access memories (FeRAMs) and dynamic random access memory (DRAM) capacitors[151,152]. Based on the Neumann–Curie principle, chiral perovskites are expected to exhibit intrinsic ferroelectric properties if they crystallize in the special point groups of C_1, C_2, C_3, C_4 and C_6. Owing to the organic and inorganic hybrid nature, the ferroelectric performance of chiral perovskites can be tuned efficiently through rational design of chiral organic ligands and the introduction of different metals[40,41,84,115].

Recently, a series of ferroelectric chiral perovskites, ranging from 3D metal-free chiral perovskites[84] to 1D chiral hybrid organic–inorganic manganese perovskites[41] and 2D chiral hybrid organic–inorganic lead perovskites[40] were reported. In 3D metal-free chiral perovskites (FIG. 8a)[84], chiral 3-ammoniopyrrolidinium (3-AP, FIG. 4a) and 3-ammonioquinuclidinium (3-AQ, FIG. 4a) were employed to introduce chirality, and the resulting *R*(or *S*)-3AP-NH_4X_3 and *R*(or *S*)-3AQ-NH_4X_3 belong to the $P2_1$ Sohncke

space group at room temperature (X=Cl or Br), thus enabling pyroelectric and ferroelectric properties[92,93].

Later, different halide atoms were introduced to obtain 1D and 2D chiral HOIPs[40,41]. Owing to the strong electron-withdrawing ability of fluorine and chlorine atoms, the electric dipole moment was enhanced, thus increasing the saturated polarization under an electric field. Moreover, the intermolecular interactions could be enhanced through hydrogen bonds and dipole–dipole interactions; thus, the ferroelectric working temperature could be increased to above room temperature.

For example, the introduction of fluorine atoms into (pyrrolidinium)$MnCl_3$[153] increased the phase transition temperature for the obtained chiral *R*-(and *S*-)3-FP-$MnCl_3$ (3-FP, FIG. 4a) to 333 K[41], compared to 295 K for the parent compound (pyrrolidinium)$MnCl_3$. The saturated polarization of *R*-3-FP-$MnCl_3$ and *S*-3-FP-$MnCl_3$ reaches 5.0 and 5.4 μC/cm^2 at 313 K, respectively, and decreases to zero after heating to the paraelectric phase at 363 K (FIG. 8b,c)[41]. Recently, this strategy was extended to 1D hybrid organic–inorganic cadmium chiral perovskites[115]: the phase transition temperature increased by 63 K after introducing fluorine, while the saturated polarization increased from 3.6 μC/cm^2 to 5.79 μC/cm^2.

Chlorine, another electron-withdrawing atom, was introduced to the para position of MBA (CMBA, FIG. 4a), and 2D chiral (*R*-CMBA)$_2$$PbI_4$ and (*S*-CMBA)$_2$$PbI_4$ were obtained (FIG. 8d)[40]. The incorporation of the chlorine atom decreases the crystal symmetry from the highly symmetric $P2_12_12_1$ space group of (*R*-MBA)$_2$$PbI_4$[34] to the lower-symmetry space group *P*1 for (*R*-CMBA)$_2$$PbI_4$; thus, (*R*-CMBA)$_2$$PbI_4$ exhibits intrinsic ferroelectricity whereas (*R*-MBA)$_2$$PbI_4$ does not. Both (*R*-CMBA)$_2$$PbI_4$ and

(*S*-CMBA)$_2$PbI$_4$ exhibit a large saturated polarization of 13.96 μC/cm^2 at 293 K based on the point charge model.

However, the above ferroelectric performances were measured on single crystals, not thin films. For commercial application, ferroelectric materials should be solution processed, which would enable integrated ferroelectric devices[151,152]. Thus, the next step is developing high-performance multiaxial ferroelectric films[154].

[H1] Outlook

Although chiral perovskites were first synthesized in the early 2000s[33], their chiroptical properties were only measured as recently as in 2017[47]. Since then, reports of chiral perovskites have become more prevalent[35,37-41,48,79-85,115,155]. As this trend continues, we expect that more researchers will begin to explore their properties, new fields will open up, and new applications will be targeted. Here, we discuss specific areas of interest for chiral perovskites.

[H2] 3D chiral perovskites

Compared to their low-dimensional counterparts, 3D chiral HOIPs should have smaller exciton binding energies and longer carrier diffusion lengths, which should prove advantageous in chiroptoelectronic and spintronic applications. As of today, however, 3D chiral HOIPs have yet to be synthesized. Recently, theoretical calculations have shown that 3D chiral perovskites should be both thermodynamically and kinetically stable[85]. These 3D chiral perovskites would contain a chiral cation such as $CHFClNH_3^+$ or $CHDFNH_3^+$. Note that these two chiral cations are the simplest known practical forms of chiral ligands, although other varieties of small chiral ligands could also be possible[156]. If they can be synthesized, we believe the resulting 3D chiral HOIPs will

find wide applications, including the production of circularly polarized perovskite waveguides[157], photodetectors[38] and lasers[158], second-order nonlinear optical imaging[61], chiro-spintronics[43,44] and topological quantum engineering[51].

[H2] Spintronic applications

Recently, it was discovered that chiral molecules can be used in the injection and detection of spin signals[43], and the combination of the spin filtering effect of molecular chirality and spintronics nurtures a new research domain, called chiro-spintronics or chiral-based spintronics[43,44].

Achiral perovskites recently showed promising spin-related properties[32], including strong spin–orbit coupling[135], large Rashba splitting[25,26,159] and long spin lifetimes[27-29]. However, they require the use of a magnetic field or of a circularly polarized excitation to generate spin-polarized carriers, whereas chiral perovskites inherently enable spin-polarized absorption and emission. In addition, chiral perovskites provide a platform for spin transport[31] and spin manipulation[30,39,83]. Recently, optical spin manipulation was demonstrated in low-dimensional chiral perovskites in the absence of an external magnetic field[83]. Chiral perovskites exhibit asymmetric circular polarization emission rates[83], which leads to an imbalanced population of different spin species of charge carrier even under continuous unpolarized excitation. This could be utilized to create a spin current either in the perovskite itself or by spin injection into a ferromagnetic material. This is in contrast to the creation of a spin imbalance in achiral materials such as achiral perovskites or transition metal dichalcogenide monolayers, where a circularly polarized excitation or an external magnetic field are required[30,135,160,161].

Another interesting way to view chirality transfer is treating it as a spintronic equivalent of doping in semiconducting electronics. Owing to the correlation between

chirality and spin selectivity, we can 'dope' materials with different handedness of chirality through rational design. Hence, making a junction between two materials with different chirality could result in a spin diode, that is, a device that allows spin currents to flow only in one direction. It is straight-forward to extend this view to a chiral-based spin transistor and, hence, a fully chiral-based spintronic circuit. Moreover, if the material is light emitting, such as chiral perovskites, this could result in spintronic photodiodes and light-emitting diodes, in which the detection of light results in a spin current, and the emission of light depends on a spin current. All these devices would work under zero magnetic field.

[H2] Chiral quantum devices

One advantage of spin-based devices over charge-based electronics is that Joule heating is minimized, resulting in more energy-efficient devices. In addition, spin (or, in general, angular momentum) represents an additional degree of freedom to carry information. Therefore, spin is one of the best candidates for the physical realization of quantum bits[66]. It has been noted that chirality may also play an important role in quantum communications[162].

For quantum communications, photon polarization is used for carrying quantum information in a variety of schemes. As such, a well-polarized and highly efficient single photon source is desired. For most well-established single-photon sources, such as InGaAs quantum dots, emission is unpolarized[163]. Subsequently polarizing the emission unavoidably reduces its efficiency. Therefore, it is an advantage that chiral perovskite quantum dots generate single photons with a well polarized state (circularly polarized). Additionally, it has been shown that chiral materials can be used to detect the orbital angular momentum of light[164], which is another degree of freedom that can

be used to record quantum information[165]. Hence, utilization of chiral perovskites could enable high-capacity quantum communication.

Furthermore, for quantum internet schemes, spins are used as qubits in each node (FIG. 1e)[166], and photons are used to connect these nodes. In this scheme, the spin–photon interface is critical. Recently it was reported that perovskite quantum dots have a non-degenerate bright triplet exciton state[167,168] that can be used as a spin qubit. Additionally, chiral perovskite quantum dots interact efficiently with light (they have high absorption coefficients and PLQYs). For these reasons, they may be an ideal platform for spin–photon interfaces and quantum networks. Chiral perovskites may also be used to tune the properties of these spin–photon interfaces. Towards this direction, spin manipulation and characterization of spin coherence times are important future steps.

[H2] Lead-free chiral perovskites

Chiral perovskites can also be partially or wholly doped by different heavy metals, resulting in two benefits. One is the direct manipulation of the fundamental properties of the perovskites. A recent review has highlighted the structure–property effects of doping in achiral perovskites[169], which could prove to be a template for the chiral variants. For chiral applications (including spintronic devices), we expect that spin–orbit coupling will play an important role in the design and tuning of the optoelectronic and spintronic properties of chiral perovskites, and the influence of different metals should be dramatic.

The second benefit is the possibility of making lead-free devices. For some applications, the presence of lead is problematic. Lead's toxicity stems from its ability to mimic other metals and interfere with biological functions. Examples include

blocking N-methyl-D-aspartate (NMDA) receptors and inhibiting the formation of heme, leading to neuron damage and anemia, respectively[170].

Therefore, its replacement with a less hazardous metal is strongly desired. For achiral perovskites, tin (Sn^{2+}) is considered to be the most promising alternative[169], as it has a similar ionic radius as lead, and tin-based solar cells have achieved power conversion efficiencies over 9%[171]. Recently, other lead-free chiral HOIPs based on bismuth[37], copper[112-114], manganese[41] and cobalt[116] have also been reported. Hybrid chiral manganese perovskites are good candidates for circularly polarized LEDs[172], and hybrid chiral copper and cobalt perovskites are attractive chiral ferromagnetic materials[173].

[H2] Machine learning and theoretical studies

In recent years, machine learning, in combination with density functional theory (DFT), has enabled the computational screening and accelerated the discovery of novel perovskite structures[174-178]. Some lead-free perovskites were predicted by theoretical calculations and then realized synthetically[179,180]. The systematic application of machine learning for the identification of novel chiral perovskite structures would accelerate discovery, but a larger library of materials is first necessary to gain predictive power. At the same time, deeper theoretical studies are still needed to predict circular dichroism, circularly polarized emission and the topological quantum properties of chiral perovskites[51,181,182]. These theoretical studies could provide more suggestions and guidance for the rational design of high-performance chiral perovskite materials and accelerate the development of chiroptics towards application.

[H2] New design strategies

The strategies for circumventing the challenges for chiral perovskites might naturally diverge from those that are currently employed. For example, changes that slightly

decrease the mobility might still be considered worthwhile if they greatly increase the circular dichroism. In addition, the desire for chirality will require novel synthetic routes to obtain larger dissymmetry factors; this will result in new structure–property/performance relationships that will influence subsequent developments and applications.

Today, most efforts on chiral HOIPs still focus on bottom-up strategies through molecular design[33,34,84]; however, 3D printing provides another strategy to construct perovskite chiral structures through bottom-up approaches. Top-down strategies towards chiral perovskite meta-surfaces are also very promising[183-186]. These approaches combine the advantages of meta-structures (strong chirality) with the impressive optical, electrical and spintronic properties of perovskites. We envision that both bottom-up and top-down strategies will continue to improve the chiral properties of HOIPs.

1 Shi, D. *et al.* Low trap-state density and long carrier diffusion in organolead trihalide perovskite single crystals. *Science* **347**, 519-522 (2015).
2 Stranks, S. D. *et al.* Electron-hole diffusion lengths exceeding 1 micrometer in an organometal trihalide perovskite absorber. *Science* **342**, 341-344 (2013).
3 Xing, G. *et al.* Long-range balanced electron- and hole-transport lengths in organic-inorganic $CH_3NH_3PbI_3$. *Science* **342**, 344-347 (2013).
4 Dong, Q. *et al.* Electron-hole diffusion lengths >175 μm in solution-grown $CH_3NH_3PbI_3$ single crystals. *Science* **347**, 967 (2015).
5 Tong, J. *et al.* Carrier lifetimes of >1 μs in Sn-Pb perovskites enable efficient all-perovskite tandem solar cells. *Science* **364**, 475 (2019).
6 Eperon, G. E. *et al.* Perovskite-perovskite tandem photovoltaics with optimized band gaps. *Science* **354**, 861-865 (2016).
7 Tsai, H. *et al.* High-efficiency two-dimensional Ruddlesden-Popper perovskite solar cells. *Nature* **536**, 312 (2016).
8 Jung, E. H. *et al.* Efficient, stable and scalable perovskite solar cells using poly(3-hexylthiophene). *Nature* **567**, 511-515 (2019).
9 Zhao, D. *et al.* Efficient two-terminal all-perovskite tandem solar cells enabled by high-quality low-bandgap absorber layers. *Nat. Energy* **3**, 1093-1100 (2018).
10 Yuan, M. *et al.* Perovskite energy funnels for efficient light-emitting diodes. *Nat. Nanotech.* **11**, 872 (2016).
11 Wang, N. *et al.* Perovskite light-emitting diodes based on solution-processed self-organized multiple quantum wells. *Nat. Photon.* **10**, 699 (2016).
12 Zhao, B. *et al.* High-efficiency perovskite–polymer bulk heterostructure light-emitting diodes. *Nat. Photon.* **12**, 783-789 (2018).

13 Li, Z. *et al.* Room-Temperature Continuous-Wave Operation of Organometal Halide Perovskite Lasers. *ACS Nano* **12**, 10968-10976 (2018).
14 Xing, G. *et al.* Low-temperature solution-processed wavelength-tunable perovskites for lasing. *Nat. Mater.* **13**, 476 (2014).
15 Zhu, H. *et al.* Lead halide perovskite nanowire lasers with low lasing thresholds and high quality factors. *Nat. Mater.* **14**, 636 (2015).
16 Zhang, Q., Ha, S. T., Liu, X., Sum, T. C. & Xiong, Q. Room-Temperature Near-Infrared High-Q Perovskite Whispering-Gallery Planar Nanolasers. *Nano Lett.* **14**, 5995-6001 (2014).
17 Zhang, H. *et al.* 2D Ruddlesden–Popper Perovskites Microring Laser Array. *Adv. Mater.* **30**, 1706186 (2018).
18 Milot, R. L. *et al.* Charge-Carrier Dynamics in 2D Hybrid Metal–Halide Perovskites. *Nano Lett.* **16**, 7001-7007 (2016).
19 Senanayak, S. P. *et al.* Understanding charge transport in lead iodide perovskite thin-film field-effect transistors. *Sci. Adv.* **3**, e1601935 (2017).
20 Kagan, C. R., Mitzi, D. B. & Dimitrakopoulos, C. D. Organic-Inorganic Hybrid Materials as Semiconducting Channels in Thin-Film Field-Effect Transistors. *Science* **286**, 945 (1999).
21 Brenner, T. M., Egger, D. A., Kronik, L., Hodes, G. & Cahen, D. Hybrid organic-inorganic perovskites: low-cost semiconductors with intriguing charge-transport properties. *Nat. Rev. Mater.* **1**, 15007 (2016).
22 Juarez-Perez, E. J. *et al.* Photoinduced giant dielectric constant in lead halide perovskite solar cells. *J. Phys. Chem. Lett.* **5**, 2390-2394 (2014).
23 Lin, Q., Armin, A., Burn, P. L. & Meredith, P. Filterless narrowband visible photodetectors. *Nat. Photon.* **9**, 687 (2015).
24 Fang, Y., Dong, Q., Shao, Y., Yuan, Y. & Huang, J. Highly narrowband perovskite single-crystal photodetectors enabled by surface-charge recombination. *Nat. Photon.* **9**, 679 (2015).
25 Niesner, D. *et al.* Giant Rashba splitting in $CH_3NH_3PbBr_3$ organic-inorganic perovskite. *Phys. Rev. Lett.* **117**, 126401 (2016).
26 Mosconi, E., Etienne, T. & De Angelis, F. Rashba Band Splitting in Organohalide Lead Perovskites: Bulk and Surface Effects. *J. Phys. Chem. Lett.* **8**, 2247-2252 (2017).
27 Odenthal, P. *et al.* Spin-polarized exciton quantum beating in hybrid organic–inorganic perovskites. *Nat. Phys.* **13**, 894 (2017).
28 Giovanni, D. *et al.* Highly Spin-Polarized Carrier Dynamics and Ultralarge Photoinduced Magnetization in $CH_3NH_3PbI_3$ Perovskite Thin Films. *Nano Lett.* **15**, 1553-1558 (2015).
29 Zheng, F., Tan, L. Z., Liu, S. & Rappe, A. M. Rashba Spin-Orbit Coupling Enhanced Carrier Lifetime in $CH_3NH_3PbI_3$. *Nano Lett.* **15**, 7794-7800 (2015).
30 Wang, J. *et al.* Spin-optoelectronic devices based on hybrid organic-inorganic trihalide perovskites. *Nat. Commun.* **10**, 129 (2019).
31 Sun, D. *et al.* Spintronics of organometal trihalide perovskites. Preprint at https://arxiv.org/abs/1608.00993 (2016).
32 Liao, K. *et al.* Spintronics of Hybrid Organic–Inorganic Perovskites: Miraculous Basis of Integrated Optoelectronic Devices. *Adv. Opt. Mater.* **7**, 1900350 (2019).
33 Billing, D. G. & Lemmerer, A. Bis[(*S*)-*b*-phenethylammonium] tribromoplumbate(II). *Acta Cryst. Sect. E* **59**, m381-m383 (2003).
The first report of a chiral organic–inorganic perovskite.
34 Billing, D. G. & Lemmerer, A. Synthesis and crystal structures of inorganic-organic hybrids incorporating an aromatic amine with a chiral functional group. *CrystEngComm* **8**, 686-695 (2006).
35 Peng, Y. *et al.* White-light emission in a chiral one-dimensional organic–inorganic hybrid perovskite. *J. Mater. Chem. C* **6**, 6033-6037 (2018).

36 Mercier, N. *et al.* Conglomerate-to-True-Racemate Reversible Solid-State Transition in Crystals of an Organic Disulfide-Based Iodoplumbate. *Angew. Chem. Int. Ed.* **45**, 2100-2103 (2006).

37 Moon, T. H., Oh, S.-J. & Ok, K. M. [((*R*)-$C_8H_{12}N)_4$][Bi_2Br_{10}] and [((*S*)-$C_8H_{12}N)_4$][Bi_2Br_{10}]: Chiral Hybrid Bismuth Bromides Templated by Chiral Organic Cations. *ACS Omega* **3**, 17895-17903 (2018).

38 Chen, C. *et al.* Circularly polarized light detection using chiral hybrid perovskite. *Nat. Commun.* **10**, 1927 (2019).

Report of chiral perovskite photodetectors with responsivity 100 times higher than that of chiral molecule photodetectors.

39 Ma, J. *et al.* Chiral 2D Perovskites with a High Degree of Circularly Polarized Photoluminescence. *ACS Nano* **13**, 3659-3665 (2019).

Report of ~17% photoluminescene polarization of 2D chiral perovskite microplates at 77 K.

40 Yang, C.-K. *et al.* The First 2D Homochiral Lead Iodide Perovskite Ferroelectrics: [*R*- and *S*-1-(4-Chlorophenyl)ethylammonium]$_2PbI_4$. *Adv. Mater.* **31**, 1808088 (2019).

41 Ai, Y. *et al.* Fluorine Substitution Induced High T_c of Enantiomeric Perovskite Ferroelectrics: (*R*)- and (*S*)-3-(Fluoropyrrolidinium)$MnCl_3$. *J. Am. Chem. Soc.* **141**, 4474-4479 (2019).

42 Liu, Y. *et al.* Chemical nature of ferroelastic twin domains in $CH_3NH_3PbI_3$ perovskite. *Nat. Mater.* **17**, 1013-1019 (2018).

43 Abendroth, J. M. *et al.* Spin Selectivity in Photoinduced Charge-Transfer Mediated by Chiral Molecules. *ACS Nano* **13**, 4928-4946 (2019).

44 Naaman, R., Paltiel, Y. & Waldeck, D. H. Chiral molecules and the electron spin. *Nat. Rev. Chem.* **3**, 250-260 (2019).

Comprehensive review of chiral-induced spin-selective effect and its applications.

45 Kelvin, W. T. *The molecular tactics of a crystal*. 26-27 (Clarendon Press, 1894).

46 Berova, N. N., Koji; Woody, Robert W. *Circular Dichorism: Principels and Applications*. 2nd edn, (Wiley-VCH, 2000).

47 Ahn, J. *et al.* A new class of chiral semiconductors: chiral-organic-molecule-incorporating organic–inorganic hybrid perovskites. *Mater. Horiz.* **4**, 851-856 (2017).

First exploration of chiroptical behaviour of chiral organic–inorganic perovskites by circular dichroism.

48 Yuan, C. *et al.* Chiral lead halide perovskite nanowires for second-order nonlinear optics. *Nano Lett.* **18**, 5411-5417 (2018).

Report of circularly polarized second-harmonic generation in chiral perovskite nanowires.

49 Naciri, J. *et al.* Synthesis and Pyroelectric Properties of Novel Ferroelectric Organosiloxane Liquid Crystalline Materials. *Chem. Mater.* **14**, 5134-5139 (2002).

50 Zhang, H.-Y., Tang, Y.-Y., Shi, P.-P. & Xiong, R.-G. Toward the Targeted Design of Molecular Ferroelectrics: Modifying Molecular Symmetries and Homochirality. *Acc. Chem. Res.* (2019).

51 Sanchez, D. S. *et al.* Topological chiral crystals with helicoid-arc quantum states. *Nature* **567**, 500-505 (2019).

52 Yang, Y., da Costa, R. C., Fuchter, M. J. & Campbell, A. J. Circularly polarized light detection by a chiral organic semiconductor transistor. *Nat. Photon.* **7**, 634 (2013).

53 Li, W. *et al.* Circularly polarized light detection with hot electrons in chiral plasmonic metamaterials. *Nat. Commun.* **6**, 8379 (2015).

54 Brandt, J. R., Salerno, F. & Fuchter, M. J. The added value of small-molecule chirality in technological applications. *Nat. Rev. Chem.* **1**, 0045 (2017).

55 Schulz, M. *et al.* Chiral Excitonic Organic Photodiodes for Direct Detection of Circular Polarized Light. *Adv. Funct. Mater.* **29**, 1900684 (2019).

56 Wu, Z.-G. *et al.* Chiral Octahydro-Binaphthol Compound-Based Thermally Activated Delayed Fluorescence Materials for Circularly Polarized Electroluminescence with Superior EQE of 32.6% and Extremely Low Efficiency Roll-Off. *Adv. Mater.* **31**, 1900524 (2019).

57 Zinna, F. *et al.* Design of Lanthanide-Based OLEDs with Remarkable Circularly Polarized Electroluminescence. *Adv. Funct. Mater.* **27**, 1603719 (2017).

58 Feuillastre, S. *et al.* Design and Synthesis of New Circularly Polarized Thermally Activated Delayed Fluorescence Emitters. *J. Am. Chem. Soc.* **138**, 3990-3993 (2016).

59 Yang, Y., da Costa, R. C., Smilgies, D.-M., Campbell, A. J. & Fuchter, M. J. Induction of Circularly Polarized Electroluminescence from an Achiral Light-Emitting Polymer via a Chiral Small-Molecule Dopant. *Adv. Mater.* **25**, 2624-2628 (2013).

60 Han, J. *et al.* Recent Progress on Circularly Polarized Luminescent Materials for Organic Optoelectronic Devices. *Adv. Opt. Mater.* **6**, 1800538 (2018).

61 Kissick, D. J., Wanapun, D. & Simpson, G. J. Second-Order Nonlinear Optical Imaging of Chiral Crystals. *Annu. Rev. Analy. Chem.* **4**, 419-437 (2011).

62 Heffern, M. C., Matosziuk, L. M. & Meade, T. J. Lanthanide Probes for Bioresponsive Imaging. *Chem. Rev.* **114**, 4496-4539 (2014).

63 Lee, H. *et al.* Chiral imaging of collagen by second-harmonic generation circular dichroism. *Biomed. Opt. Express* **4**, 909-916 (2013).

64 Bisoyi, H. K. & Li, Q. Light-Directing Chiral Liquid Crystal Nanostructures: From 1D to 3D. *Acc. Chem. Res.* **47**, 3184-3195 (2014).

65 Schadt, M. Liquid Crystal Materials and Liquid Crystal Displays. *Annu. Rev. Mater. Sci.* **27**, 305-379 (1997).

66 Nielsen, M. A. & Chuang, I. L. *Quantum Computation and Quantum Information: 10th Anniversary Edition*. (Cambridge University Press, 2011).

67 Service, R. F. Lighting the Way to a Quantum Computer. *Science* **292**, 2412 (2001).

68 Gisin, N. & Thew, R. Quantum communication. *Nat. Photon.* **1**, 165 (2007).

69 Liao, S.-K. *et al.* Satellite-Relayed Intercontinental Quantum Network. *Phys. Rev. Lett.* **120**, 030501 (2018).

70 Humphreys, P. C. *et al.* Deterministic delivery of remote entanglement on a quantum network. *Nature* **558**, 268-273 (2018).

71 Chang, K. *et al.* Discovery of robust in-plane ferroelectricity in atomic-thick SnTe. *Science* **353**, 274 (2016).

72 Kepenekian, M. *et al.* Rashba and Dresselhaus Effects in Hybrid Organic–Inorganic Perovskites: From Basics to Devices. *ACS Nano* **9**, 11557-11567 (2015).

73 Lee, D.-M., Song, J.-W., Lee, Y.-J., Yu, C.-J. & Kim, J.-H. Control of Circularly Polarized Electroluminescence in Induced Twist Structure of Conjugate Polymer. *Adv. Mater.* **29**, 1700907 (2017).

74 Wan, L. *et al.* Inverting the Handedness of Circularly Polarized Luminescence from Light-Emitting Polymers Using Film Thickness. *ACS Nano* **13**, 8099-8105 (2019).

75 Dor, O. B., Yochelis, S., Mathew, S. P., Naaman, R. & Paltiel, Y. A chiral-based magnetic memory device without a permanent magnet. *Nat. Commun.* **4**, 2256 (2013).

76 Ben Dor, O. *et al.* Magnetization switching in ferromagnets by adsorbed chiral molecules without current or external magnetic field. *Nat. Commun.* **8**, 14567 (2017).

77 Lee, M. M., Teuscher, J., Miyasaka, T., Murakami, T. N. & Snaith, H. J. Efficient Hybrid Solar Cells Based on Meso-Superstructured Organometal Halide Perovskites. *Science* **338**, 643-647 (2012).

78 Kim, H.-S. *et al.* Lead Iodide Perovskite Sensitized All-Solid-State Submicron Thin Film Mesoscopic Solar Cell with Efficiency Exceeding 9%. *Sci. Rep.* **2**, 591 (2012).

79 He, T. *et al.* Spectroscopic studies of chiral perovskite nanocrystals. *Appl. Phys. Lett.* **111**, 151102 (2017).

80 Chen, W. *et al.* Two-Photon Absorption-Based Upconverted Circularly Polarized Luminescence Generated in Chiral Perovskite Nanocrystals. *J. Phys. Chem. Lett.*, 3290-3295 (2019).

Report of the first two-photon absorption-based upconverted circularly polarized photoluminescence.

81 Shi, Y., Duan, P., Huo, S., Li, Y. & Liu, M. Endowing perovskite nanocrystals with circularly polarized luminescence. *Adv. Mater.* **30**, 1705011 (2018).

82 Georgieva, Z. N., Bloom, B. P., Ghosh, S. & Waldeck, D. H. Imprinting chirality onto the electronic states of colloidal perovskite nanoplatelets. *Adv. Mater.* **30**, 1800097 (2018).

83 Long, G. *et al.* Spin control in reduced-dimensional chiral perovskites. *Nat. Photon.* **12**, 528-533 (2018).

Report of low-dimensional chiral perovskites exhibiting 3% circularly polarized photoluminescence without an external magnetic field.

84 Ye, H.-Y. *et al.* Metal-free three-dimensional perovskite ferroelectrics. *Science* **361**, 151-155 (2018).

Report of the first metal-free 3D chiral perovskites.

85 Long, G. *et al.* Theoretical Prediction of Chiral 3D Hybrid Organic–Inorganic Perovskites. *Adv. Mater.* **31**, 1807628 (2019).

Theoretical prediction that 3D chiral organic–inorganic perovskites are thermodynamically and kinetically stable.

86 Dong, Y. *et al.* Chiral Perovskites: Promising Materials toward Next-Generation Optoelectronics. *Small* **15**, 1902237 (2019).

87 Fischer, P. & Hache, F. Nonlinear optical spectroscopy of chiral molecules. *Chirality* **17**, 421-437 (2005).

88 Shi, P.-P. *et al.* Symmetry breaking in molecular ferroelectrics. *Chem. Soc. Rev.* **45**, 3811-3827 (2016).

89 Mujica, V. Chirality transfer takes a jump. *Nat. Chem.* **7**, 543 (2015).

90 Ostovar pour, S. *et al.* Through-space transfer of chiral information mediated by a plasmonic nanomaterial. *Nat. Chem.* **7**, 591 (2015).

91 Sohncke, L. *Entwickelung einer Theorie der Krystallstruktur*. (B. G. Teubner, 1879).

92 Neumann, F. E. & Meyer, O. E. *Vorlesungen über die Theorie der Elasticität der festen Körper und des Lichtäthers, gehalten an der Universität Königsberg*. (B. G. Teubner, 1885).

93 Curie, P. Sur la symétrie dans les phénomènes physiques, symétrie d'un champ électrique et d'un champ magnétique. *J. Phys. Theor. Appl.* **3**, 393-415 (1894).

94 Halasyamani, P. S. & Poeppelmeier, K. R. Noncentrosymmetric Oxides. *Chem. Mater.* **10**, 2753-2769 (1998).

95 Nespolo, M., Aroyo, M. I. & Souvignier, B. Crystallographic shelves: space-group hierarchy explained. *J. Appl. Crystallogr.* **51**, 1481-1491 (2018).

96 Ma, W. *et al.* Chiral Inorganic Nanostructures. *Chem. Rev.* **117**, 8041-8093 (2017).

97 Lightner, D. A. G., J. E. Organic conformational analysis and stereochemistry from circular dichroism spectroscopy. (2010).

98 Polavarapu, P. L. Kramers−Kronig Transformation for Optical Rotatory Dispersion Studies. *J. Phys. Chem. A* **109**, 7013-7023 (2005).

99 Li, A. D. & Liu, W. C. in *Physical Properties and Applications of Polymer Nanocomposites* (eds S. C. Tjong & Y. W. Mai) 108-158 (Woodhead Publishing, 2010).

100 Liao, W.-Q., Tang, Y.-Y., Li, P.-F., You, Y.-M. & Xiong, R.-G. Competitive Halogen Bond in the Molecular Ferroelectric with Large Piezoelectric Response. *J. Am. Chem. Soc.* **140**, 3975-3980 (2018).

101 Li, Y., Yu, D., Dai, L., Urbas, A. & Li, Q. Organo-Soluble Chiral Thiol-Monolayer-Protected Gold Nanorods. *Langmuir* **27**, 98-103 (2011).

102 Dolamic, I., Knoppe, S., Dass, A. & Bürgi, T. First enantioseparation and circular dichroism spectra of Au_{38} clusters protected by achiral ligands. *Nat. Commun.* **3**, 798 (2012).

103 Goldsmith, M.-R. *et al.* The chiroptical signature of achiral metal clusters induced by dissymmetric adsorbates. *Phys. Chem. Chem. Phys.* **8**, 63-67 (2006).

104 Carmeli, I. *et al.* Broad Band Enhancement of Light Absorption in Photosystem I by Metal Nanoparticle Antennas. *Nano Lett.* **10**, 2069-2074 (2010).

105 Lemmerer, A. & Billing, D. G. Inorganic-Organic Hybrids Incorporating a Chiral Cyclic Ammonium Cation. *S. Afr. J. Chem.* **66**, 263-272 (2013).

106 Yuan, Z. *et al.* One-dimensional organic lead halide perovskites with efficient bluish white-light emission. *Nat. Commun.* **8**, 14051 (2017).

107 Hu, T. *et al.* Mechanism for Broadband White-Light Emission from Two-Dimensional (110) Hybrid Perovskites. *J. Phys. Chem. Lett.* **7**, 2258-2263 (2016).

108 Peng, Y. *et al.* Exploration of Chiral Organic–Inorganic Hybrid Semiconducting Lead Halides. *Chem. Asian J.* **14**, 2273-2277 (2019).

109 Zhu, L.-L. *et al.* Stereochemically active lead chloride enantiomers mediated by homochiral organic cation. *Polyhedron* **158**, 445-448 (2019).

110 Black, R. S. & Billing, D. G. The structure and photoluminescence of chiral tin and lead inorganic-organic hybrid perovskites. *Acta Cryst. Sect. A* **64**, C455-C456 (2008).

111 Black, R. S. Structure and Optical Properties of Natural Low Dimensional, Semiconducting, Organic Inorganic Hybrids. *University of the Witwatersrand, Johannesburg* (2012).

112 Hajlaoui, F. *et al.* Synthesis, crystal structures, second harmonic generation response and temperature phase transitions of two noncentrosymmetric Cu(II)-hybrid halides compounds: [(*R*)-$C_7H_{16}N_2$][CuX_4] (X = Cl or Br). *J. Mol. Struct.* **1182**, 47-53 (2019).

113 Ben Salah, A. M., Sayari, N., Naïli, H. & Norquist, A. J. Chiral and achiral copper(ii) complexes: structure, bonding and biological activities. *RSC Adv.* **6**, 59055-59065 (2016).

114 Mande, H. M., Ghalsasi, P. S. & Navamoney, A. Synthesis, structural and spectroscopic characterization of the thermochromic compounds A_2CuCl_4: [(Naphthyl ethylammonium)$_2CuCl_4$]. *Polyhedron* **91**, 141-149 (2015).

115 Tang, Y.-Y. *et al.* H/F-Substitution-Induced Homochirality for Designing High-T_c Molecular Perovskite Ferroelectrics. *Adv. Mater.* **31**, 1902163 (2019).

116 Mande, H. M., Ghalsasi, P. S. & Arulsamy, N. Racemic and conglomerate 1-(4-haloaryl)ethylammonium tetrachlorocobaltate salts: formation of helical structures. *RSC Adv.* **5**, 62719-62723 (2015).

117 Gao, X., Han, B., Yang, X. & Tang, Z. Perspective of Chiral Colloidal Semiconductor Nanocrystals: Opportunity and Challenge. *J. Am. Chem. Soc.* **141**, 13700-13707 (2019).

118 Zhao, H.-R., Li, D.-P., Ren, X.-M., Song, Y. & Jin, W.-Q. Larger Spontaneous Polarization Ferroelectric Inorganic−Organic Hybrids: $[PbI_3]_\infty$ Chains Directed Organic Cations Aggregation to Kagomé-Shaped Tubular Architecture. *J. Am. Chem. Soc.* **132**, 18-19 (2010).

119 Tong, Y. *et al.* Highly Luminescent Cesium Lead Halide Perovskite Nanocrystals with Tunable Composition and Thickness by Ultrasonication. *Angew. Chem. Int. Ed.* **55**, 13887-13892 (2016).

120 Xue, S., Xing, P., Zhang, J., Zeng, Y. & Zhao, Y. Diverse Role of Solvents in Controlling Supramolecular Chirality. *Chem-Asian J.* **25**, 7426-7437 (2019).

121 Rickhaus, M., Mayor, M. & Juríček, M. Strain-induced helical chirality in polyaromatic systems. *Chem. Soc. Rev.* **45**, 1542-1556 (2016).

122 Kuzyk, A. *et al.* DNA-based self-assembly of chiral plasmonic nanostructures with tailored optical response. *Nature* **483**, 311 (2012).

123 Yashima, E. *et al.* Supramolecular Helical Systems: Helical Assemblies of Small Molecules, Foldamers, and Polymers with Chiral Amplification and Their Functions. *Chem. Rev.* **116**, 13752-13990 (2016).

124 Huck, N. P. M., Jager, W. F., de Lange, B. & Feringa, B. L. Dynamic Control and Amplification of Molecular Chirality by Circular Polarized Light. *Science* **273**, 1686 (1996).

125 Moss, G. P. Basic terminology of stereochemistry (IUPAC Recommendations 1996). *Pure Appl. Chem.* **68**, 2193 (1996).
126 Zheng, H. *et al.* Uncovering the Circular Polarization Potential of Chiral Photonic Cellulose Films for Photonic Applications. *Adv. Mater.* **30**, 1705948 (2018).
127 Schellman, J. A. & Oriel, P. Origin of the Cotton Effect of Helical Polypeptides. *J. Chem. Phys.* **37**, 2114-2124 (1962).
128 Rochat, E., Walker, S. D. & Parker, M. C. Polarisation and wavelength division multiplexing at 1.55μm for bandwidth enhancement of multimode fibre based access networks. *Opt. Express* **12**, 2280-2292 (2004).
129 Yang, Y. *et al.* Emergent Properties of an Organic Semiconductor Driven by its Molecular Chirality. *ACS Nano* **11**, 8329-8338 (2017).
130 Liu, H. L. *et al.* 3D chiral color prints for anti-counterfeiting. *Nanoscale* **11**, 5506-5511 (2019).
131 Brandt, J. R., Wang, X., Yang, Y., Campbell, A. J. & Fuchter, M. J. Circularly Polarized Phosphorescent Electroluminescence with a High Dissymmetry Factor from PHOLEDs Based on a Platinahelicene. *J. Am. Chem. Soc.* **138**, 9743-9746 (2016).
132 Cao, Y. *et al.* Perovskite light-emitting diodes based on spontaneously formed submicrometre-scale structures. *Nature* **562**, 249-253 (2018).
133 Lin, K. *et al.* Perovskite light-emitting diodes with external quantum efficiency exceeding 20 per cent. *Nature* **562**, 245-248 (2018).
134 Xing, G. *et al.* Transcending the slow bimolecular recombination in lead-halide perovskites for electroluminescence. *Nat. Commun.* **8**, 14558 (2017).
135 Zhang, C. *et al.* Magnetic field effects in hybrid perovskite devices. *Nat. Phys.* **11**, 427 (2015).
136 Hilborn, R. C. Einstein coefficients, cross sections, f values, dipole moments, and all that. *Am. J. Phys.* **50**, 982-986 (1982).
137 Minzioni, P. *et al.* Roadmap on all-optical processing. *J. Opt.* **21**, 063001 (2019).
138 Zipfel, W. R., Williams, R. M. & Webb, W. W. Nonlinear magic: multiphoton microscopy in the biosciences. *Nat. Biotechnol.* **21**, 1369-1377 (2003).
139 Stoumpos, C. C. *et al.* Ruddlesden–Popper Hybrid Lead Iodide Perovskite 2D Homologous Semiconductors. *Chem. Mater.* **28**, 2852-2867 (2016).
140 Li, L. *et al.* Bilayered Hybrid Perovskite Ferroelectric with Giant Two-Photon Absorption. *J. Am. Chem. Soc.* **140**, 6806-6809 (2018).
141 Gao, Y. *et al.* Electro-Optic Modulation in Hybrid Metal Halide Perovskites. *Adv. Mater.* **31**, 1808336 (2019).
142 Kalanoor, B. S. *et al.* Third-Order Optical Nonlinearities in Organometallic Methylammonium Lead Iodide Perovskite Thin Films. *ACS Photon.* **3**, 361-370 (2016).
143 Zhang, R. *et al.* Nonlinear Optical Response of Organic–Inorganic Halide Perovskites. *ACS Photon.* **3**, 371-377 (2016).
144 Quan, L. N., Kang, J., Ning, C.-Z. & Yang, P. Nanowires for Photonics. *Chem. Rev.* **119**, 9153-9169 (2019).
145 Fu, Y. *et al.* Metal halide perovskite nanostructures for optoelectronic applications and the study of physical properties. *Nat. Rev. Mater.* **4**, 169-188 (2019).
146 Abel, S. *et al.* Large Pockels effect in micro- and nanostructured barium titanate integrated on silicon. *Nat. Mater.* **18**, 42-47 (2019).
147 Fang, L. *et al.* Ultra-directional high-efficiency chiral silicon photonic circuits. *Optica* **6**, 61-66 (2019).
148 Olesiak-Banska, J., Waszkielewicz, M., Obstarczyk, P. & Samoc, M. Two-photon absorption and photoluminescence of colloidal gold nanoparticles and nanoclusters. *Chem. Soc. Rev.* **48**, 4087-4117 (2019).
149 Yang, X., Yang, M., Pang, B., Vara, M. & Xia, Y. Gold Nanomaterials at Work in Biomedicine. *Chem. Rev.* **115**, 10410-10488 (2015).
150 Boyd, R. W. in *Nonlinear Optics (Third Edition)* (ed Robert W. Boyd) 69-133 (Academic Press, 2008).
151 Scott, J. F. Applications of Modern Ferroelectrics. *Science* **315**, 954-959 (2007).

152 Chen, A. A review of emerging non-volatile memory (NVM) technologies and applications. *Solid-State Electron.* **125**, 25-38 (2016).
153 Zhang, Y. *et al.* Highly Efficient Red-Light Emission in An Organic–Inorganic Hybrid Ferroelectric: (Pyrrolidinium)$MnCl_3$. *J. Am. Chem. Soc.* **137**, 4928-4931 (2015).
154 Tang, Y.-Y. *et al.* Multiaxial Molecular Ferroelectric Thin Films Bring Light to Practical Applications. *J. Am. Chem. Soc.* **140**, 8051-8059 (2018).
155 Huang, P.-J., Taniguchi, K. & Miyasaka, H. Bulk Photovoltaic Effect in a Pair of Chiral–Polar Layered Perovskite-Type Lead Iodides Altered by Chirality of Organic Cations. *J. Am. Chem. Soc.* **141**, 14520-14523 (2019).
156 Huang, S. *et al.* Halogenated-Methylammonium Based 3D Halide Perovskites. *Adv. Mater.* **31**, 1903830 (2019).
157 Guy, S., Baguenard, B., Bensalah-Ledoux, A., Hadiouche, D. & Guy, L. Full Polarization Control of Optical Planar Waveguides with Chiral Material. *ACS Photon.* **4**, 2916-2922 (2017).
158 Cerdán, L. *et al.* Circularly polarized laser emission in optically active organic dye solutions. *Phys. Chem. Chem. Phys.* **19**, 22088-22093 (2017).
159 Niesner, D. *et al.* Structural fluctuations cause spin-split states in tetragonal (CH_3NH_3)PbI_3 as evidenced by the circular photogalvanic effect. *Proc. Natl. Acad. Sci. U.S.A.* **115**, 9509 (2018).
160 Xiao, D., Liu, G.-B., Feng, W., Xu, X. & Yao, W. Coupled Spin and Valley Physics in Monolayers of MoS_2 and Other Group-VI Dichalcogenides. *Phys. Rev. Lett.* **108**, 196802 (2012).
161 Srivastava, A. *et al.* Valley Zeeman effect in elementary optical excitations of monolayer WSe_2. *Nat. Phys.* **11**, 141 (2015).
162 Lodahl, P. *et al.* Chiral quantum optics. *Nature* **541**, 473 (2017).
163 Bayer, M. *et al.* Fine structure of neutral and charged excitons in self-assembled In(Ga)As/(Al)GaAs quantum dots. *Phys. Rev. B* **65**, 195315 (2002).
164 Woźniak, P., De Leon, I., Höflich, K., Leuchs, G. & Banzer, P. Interaction of light carrying orbital angular momentum with a chiral dipolar scatterer. *Optica* **6**, 961-965 (2019).
165 Mirhosseini, M. *et al.* High-dimensional quantum cryptography with twisted light. *New J. Phys.* **17**, 033033 (2015).
166 Kimble, H. J. The quantum internet. *Nature* **453**, 1023-1030 (2008).
167 Becker, M. A. *et al.* Bright triplet excitons in caesium lead halide perovskites. *Nature* **553**, 189 (2018).
168 Tamarat, P. *et al.* The ground exciton state of formamidinium lead bromide perovskite nanocrystals is a singlet dark state. *Nat. Mater.* **18**, 717-724 (2019).
169 Zhang, X., Li, L., Sun, Z. & Luo, J. Rational chemical doping of metal halide perovskites. *Chem. Soc. Rev.* **48**, 517-539 (2019).
170 Sanders, T., Liu, Y., Buchner, V. & Tchounwou, P. B. Neurotoxic Effects and Biomarkers of Lead Exposure: A Review. *Rev. Environ. Health* **24**, 15 (2009).
171 Jokar, E., Chien, C.-H., Tsai, C.-M., Fathi, A. & Diau, E. W.-G. Robust Tin-Based Perovskite Solar Cells with Hybrid Organic Cations to Attain Efficiency Approaching 10%. *Adv. Mater.* **31**, 1804835 (2019).
172 Xu, L.-J., Sun, C.-Z., Xiao, H., Wu, Y. & Chen, Z.-N. Green-Light-Emitting Diodes based on Tetrabromide Manganese(II) Complex through Solution Process. *Adv. Mater.* **29**, 1605739 (2017).
173 Mitzi, D. B. Synthesis, Structure, and Properties of Organic-Inorganic Perovskites and Related Materials. *Prog. Inorg. Chem.* **48**, 121 (2007).
174 Lu, S. *et al.* Accelerated discovery of stable lead-free hybrid organic-inorganic perovskites via machine learning. *Nat. Commun.* **9**, 3405 (2018).
175 Kim, C., Huan, T. D., Krishnan, S. & Ramprasad, R. A hybrid organic-inorganic perovskite dataset. *Sci. Data* **4**, 170057 (2017).

176 Körbel, S., Marques, M. A. L. & Botti, S. Stability and electronic properties of new inorganic perovskites from high-throughput ab initio calculations. *J. Mater. Chem. C* **4**, 3157-3167 (2016).
177 Takahashi, K., Takahashi, L., Miyazato, I. & Tanaka, Y. Searching for Hidden Perovskite Materials for Photovoltaic Systems by Combining Data Science and First Principle Calculations. *ACS Photon.* **5**, 771-775 (2018).
178 Davies, D. W. *et al.* Computational Screening of All Stoichiometric Inorganic Materials. *Chem* **1**, 617-627 (2016).
179 Shi, Z. J. *et al.* Lead-Free Organic-Inorganic Hybrid Perovskites for Photovoltaic Applications: Recent Advances and Perspectives. *Adv. Mater.* **29** (2017).
180 Xiao, Z., Song, Z. & Yan, Y. From Lead Halide Perovskites to Lead-Free Metal Halide Perovskites and Perovskite Derivatives. *Adv. Mater.* **31**, 1803792 (2019).
181 Yu, Z.-G. Oscillatory Magnetic Circular Dichroism of Free-Carrier Absorption and Determination of the Rashba Dispersions in Hybrid Organic–Inorganic Perovskites. *J. Phys. Chem. Lett.* **9**, 1-7 (2018).
182 Tepliakov, N. V. *et al.* Optical Activity and Circular Dichroism of Perovskite Quantum-Dot Molecules. *J. Phys. Chem. C* **123**, 2658-2664 (2019).
183 Gholipour, B. *et al.* Organometallic Perovskite Metasurfaces. *Adv. Mater.* **29**, 1604268 (2017).
184 Wang, Z., Wang, Y., Adamo, G., Teng, J. & Sun, H. Induced Optical Chirality and Circularly Polarized Emission from Achiral CdSe/ZnS Quantum Dots via Resonantly Coupling with Plasmonic Chiral Metasurfaces. *Laser Photonics Rev.* **13**, 1800276 (2019).
185 Makarov, S. V. *et al.* Multifold Emission Enhancement in Nanoimprinted Hybrid Perovskite Metasurfaces. *ACS Photon.* **4**, 728-735 (2017).
186 Zhang, C. *et al.* Lead Halide Perovskite-Based Dynamic Metasurfaces. *Laser Photonics Rev.* **13**, 1900079 (2019).

Acknowledgements

W.G., G.K.L. and A.S. acknowledge the support from the Singapore National Research Foundation through 2015 NRF fellowship grant (NRF-NRFF2015-03), Singapore Ministry of Education via AcRF Tier2 grant (No. MOE2016-T2-2-077, No. MOE2017-T2-1-163), and A*Star QTE Programme. R.S and G.L. acknowledge the support from the Australian Research Council Centre of Excellence in Exciton Science (Funding grant number CE170100026). E.H.S. acknowledges support from the U.S. Office of Naval Research (grant award no.: N00014-17-1-2524). We thank Prof. Mingtao Zhang (Nankai University) for helpful discussions.

Author contributions

W.G., G.K.L. and E.H.S. discussed the content. G.K.L. researched the data for the article with help from R.S. and M.I.S., all authors contributed to the review and editing of the manuscript.

Competing financial interests

The authors declare no competing financial interests.

Supplementary information is available in the online version of the paper.

Publisher's note: Springer Nature remains neutral with regard to jurisdictional claims in published maps and institutional affiliations.

Table 1 | Chirality transfer mechanisms, dimensionality, form and applications of chiral perovskites.

Chemical formula	Mechanism	Dimensionality	Form	Application
(*R*-MBA)$_2$PbI$_4$[34,39]	I	2D	microplates	CPL source
(*R*-CMBA)$_2$PbI$_4$[40]	I	2D	crystal	Ferroelectric
R-3-FP-MnCl$_3$[41]	I	1D	crystal	Ferroelectric
(*R*-MPEA)$_{1.5}$ PbBr$_{3.5}$(DMSO)$_{0.5}$[48]	I	2D	crystal	NLO, CP-SHG
(*R*-3APD)PbCl$_4$·H$_2$O[35]	I	1D	crystal	White-light source
R-MBAPbI$_3$[38]	II	1D	film	CPL photodetector
R-LDCP[83]	II	quasi-2D	film	Spintronics
R-Pero-NCs[80]	II	0D	colloidal nanocrystal	NLO, TP-UCPPL
R-DACH-NCs[79]	II	0D	colloidal nanocrystal	CPL photodetector
Pero-NCs (DGAm)[81]	II	0D	chiral cogel	CPL source
R-MBA-NPs[82]	IV	0D	colloidal nanoplatelets	CPL photodetector

CPL: circularly polarized light; NLO: nonlinear optics; CP: circularly polarized; SHG: second-harmonic generation; DMSO: dimethyl sulfoxide; NCs: Nanocrystals; TP-UCPPL: two-photon absorption-based upconverted circularly polarized photoluminescence. Mechanisms: I, ligand-induced chiral inorganic

structure; II, chiral distortion of the inorganic surface; III chiral patterning of the surface ligands; IV, chiral field effect.

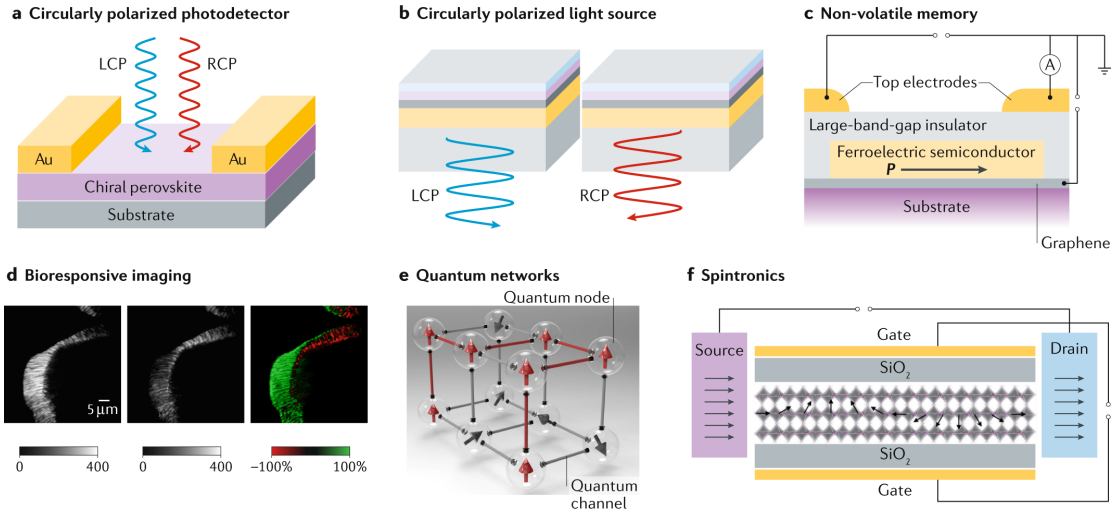

Fig. 1 | **Potential applications of chiral materials**. **a** | Circularly polarized photodetectors distinguish left-handed and right-handed circularly polarized light (LCP and RCP, respectively). **b** | Circularly polarized light sources can emit left-handed or right-handed circularly polarized light. **c** | Non-volatile memory devices can be built based on ferroelectric chiral materials with in-plane polarization *P*. **d** | In bioresponsive imaging, biological tissues respond differently to left-handed and right-handed circularly polarized excitations. The upper panel shows, from left to right, second-harmonic generation (SHG) images of a ligament excited by LCP light, RCP light, and the SHG circular dichroism image (refer Equation 4 and related discussion below for more information). Compared with the traditional SHG, polarization-resolved SHG exhibits higher contrast, which is beneficial towards imaging application and provides more underlying collagen molecular properties. **e** | In quantum networks, spins are used as qubits in each node, and photons are used as connections to build the quantum network. Chiral materials can be used as transducers between the spin and quantum states of light at each node of a quantum network. **f** | Spin field-effect transistor based on chiral perovskites. The spin precession from source to drain is controlled by the gate

voltage. Owing to strong spin–orbit coupling in perovskites, chirality is strongly correlated with spin; thus, chiral perovskites can be used as spin current injectors and spin filters. Panel **b** is reproduced with permission from REF.[59], Wiley-VCH. Panel **c** is reproduced with permission from REF.[71], AAAS. Panel **d** is reproduced with permission from REF.[63], OSA Publishing. Panel **f** is reproduced with permission from REF.[72], ACS.

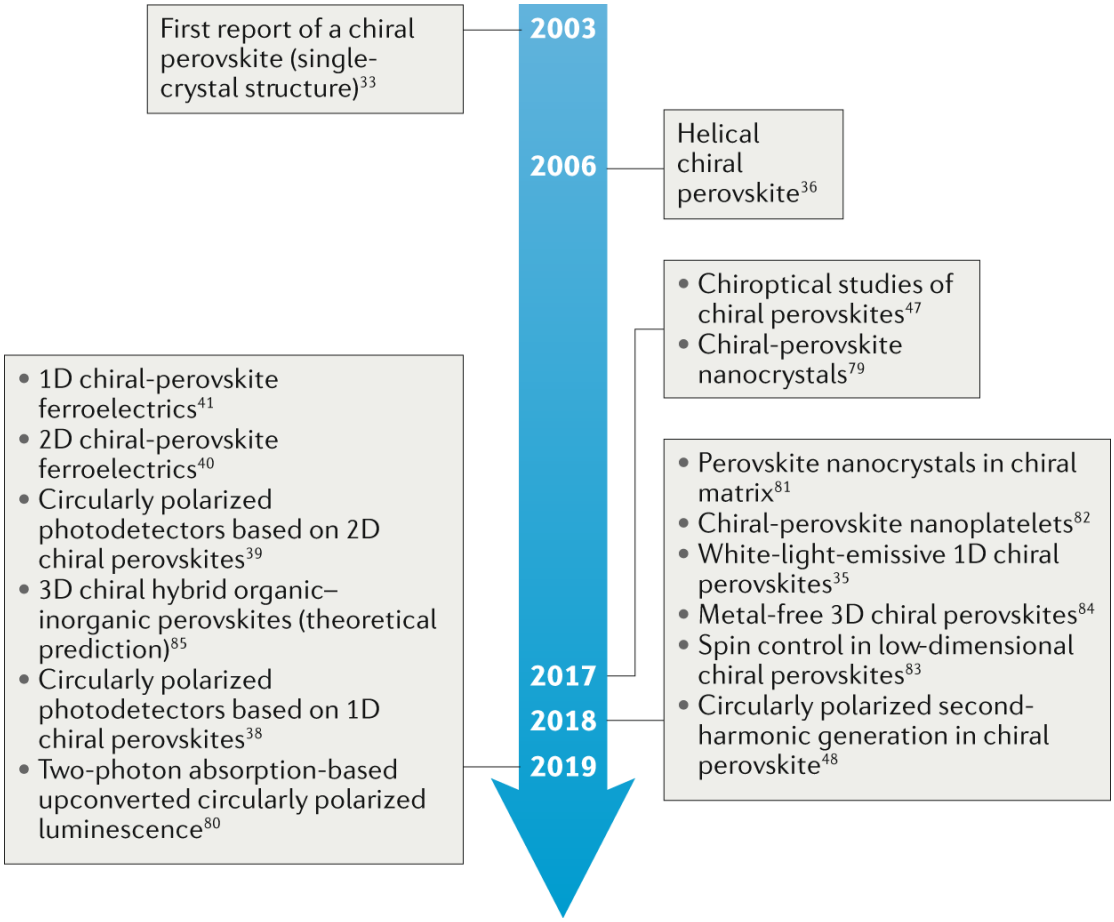

FIG. 2 | Timeline of research on chiral perovskites.

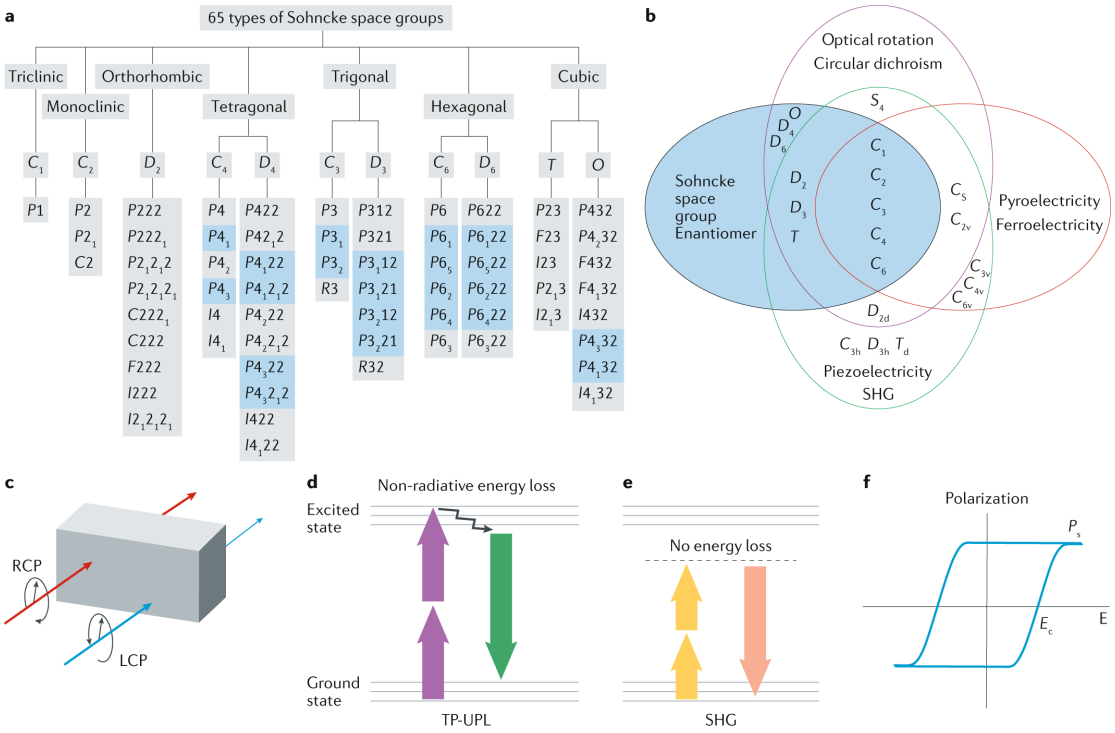

FIG. 3 | Basics of chiral material properties. a | There are 65 types of Sohncke space groups within different Bravais lattices and point groups. Chiral space groups are highlighted in blue; crystal structures belonging to the 65 listed Sohncke space groups are chiral. **b** | The Neumann-Curie principle determines the structure–property relationship of non-centrosymmetric crystals. **c** | Circular dichroism is a phenomenon whereby a material absorbs more of one circular polarized light than the other (in this example left-handed circularly polarized, LCP, rather than right-handed circularly polarized, RCP, light). **d** | Schematic representation of two-photon absorption-based upconverted photoluminescence (TP-UPL) and **e** | second harmonic generation (SHG) processes. **f** | Ferroelectric polarization vs. electrical field E hysteresis loop for ferroelectric materials; the saturated polarization (P_s) and coercivity (E_c) are marked. Panel **b** is reproduced with permission from REF.[94], ACS.

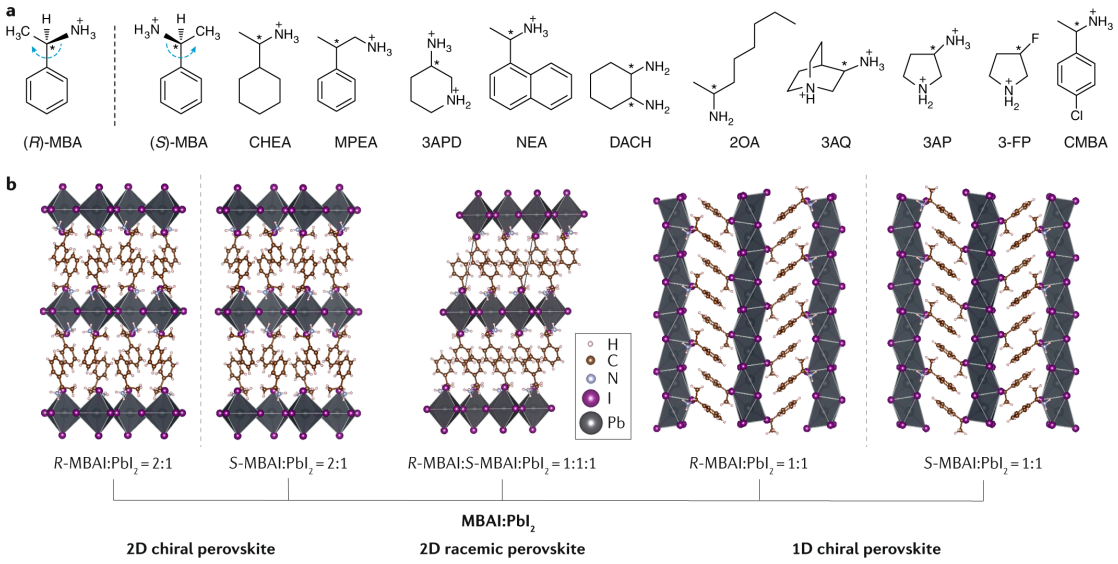

Fig. 4 | **Representative chiral ligands and chiral hybrid organic–inorganic perovskites. a** | The chiral ligands discussed in this Review: MBA (methylbenzylammonium), CHEA (1-cyclohexylethylammonium), MPEA (*β*-methylphenethylammonium), 3APD (3-aminopiperidine), NEA (1-(1-naphthyl)ethylammonium), DACH (1,2-diaminocyclohexane), 2OA (2-octylamine), 3AQ (3-ammonioquinuclidinium), 3AP (3-ammoniopyrrolidinium), 3-FP (3-fluoropyrrolidinium) and CMBA (1-(4-chlorophenyl)ethylammonium). Based on the Cahn–Ingold–Prelog (CIP) priority rules, the four groups around a chiral center are prioritized according to the atomic number and priority. This begins with the four atoms closest to the chiral center and moves to subsequent atoms in the event of a tie. With the fourth (the lowest priority) group facing away from the viewer, a path can be traced from groups 1-2-3. If this path is clockwise, the chiral center is designated as *R* (from the Latin word rectus); conversely, if it is counter clockwise, the chiral center is designated as *S* (from the Latin word sinister). Here, using (*R*)-MBA and (*S*)-MBA enantiomers as an example, the clockwise and anti-clockwise directions are shown (blue arrow) according to the priority of the four groups. **b** | Single-crystal structures of

2D and 1D chiral perovskites and of a 2D racemic achiral perovskite based on MBA: (*R*-MBA)$_2$PbI$_4$, (*S*-MBA)$_2$PbI$_4$, *R*-MBAPbI$_3$, *S*-MBAPbI$_3$ and (*rac*-MBA)$_2$PbI$_4$.

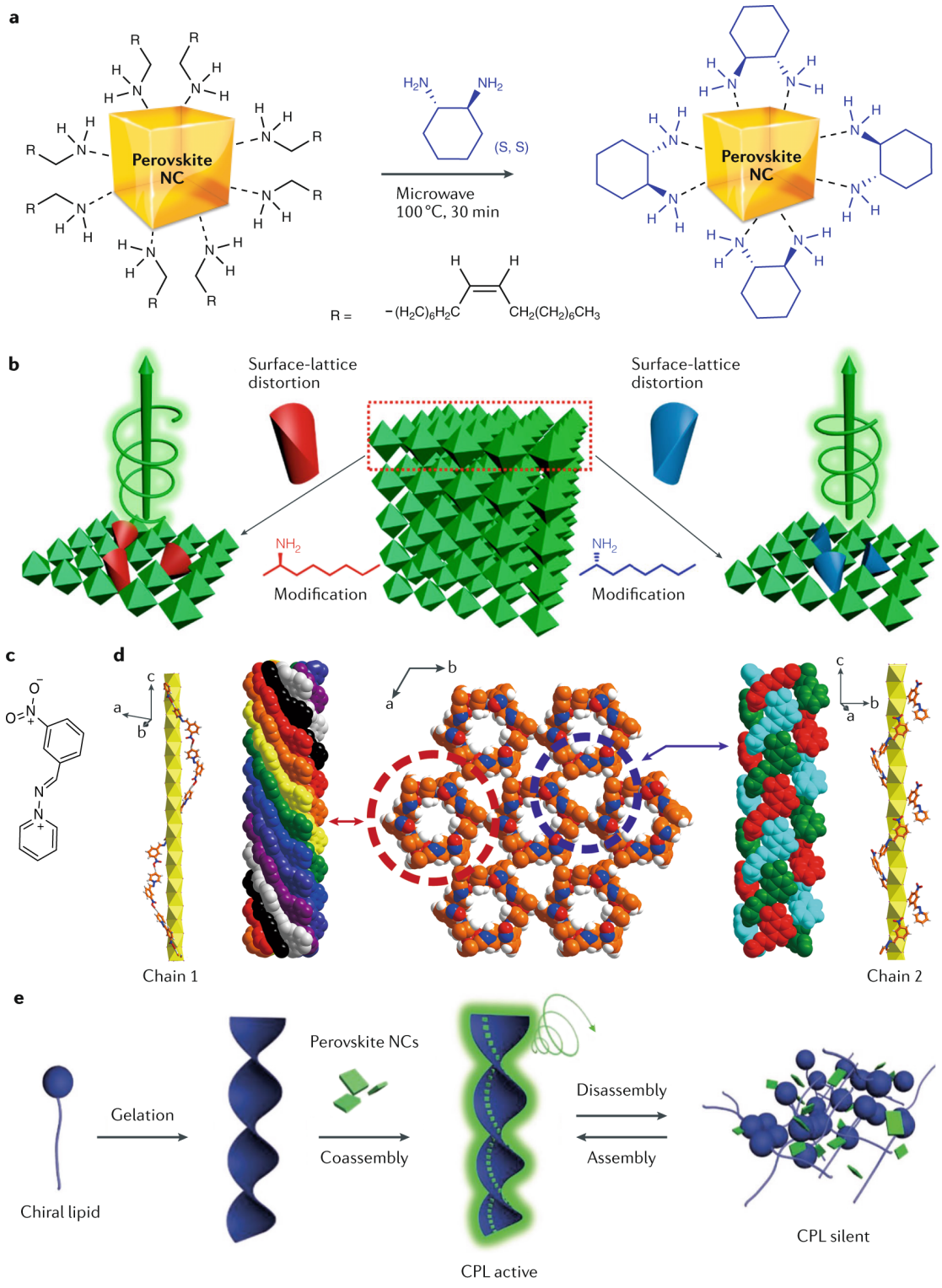

Fig. 5 | **Chirality through chiral ligands and environment. a** | Post-synthetic chiral ligand exchange strategy to synthesize chiral perovskite nanocrystals (NCs). **b** |

Schematic illustration of employing chiral-ligand-assisted tip sonication method to prepare chiral perovskite nanocrystals. Through adding the chiral ligands (left: *R*-2-octylamine, right: *S*-2-octylamine) during the direct tip sonication process, the chirality is introduced to the perovskite nanocrystal through surface lattice distortion by the chiral ligands. **c** | The molecular structure of the achiral Schiff base cation: (*E*)-1-((3-nitrobenzylidene)amino)pyridin-1-ium. **d** | The achiral (*E*)-1-((3-nitrobenzylidene)amino)pyridin-1-ium cations adopt a kagome-like tubular architecture: nonuple stranded helices around the highly polarized 1D $[PbI_3]_\infty$ chains (chain 1, sixfold screw axis) and triple stranded helices around the highly polarized 1D $[PbI_3]_\infty$ chains (chain 2, C_3 rotation axis). **e** | In the supramolecular chiral induction approach, achiral perovskite nanocrystals follow the chirality of a gel structure to produce a chiral cogel. These co-assembled structures emit circularly polarized light (CPL); the CPL signal is switched via heating or cooling the cogel, as the disassembled state obtained by heating does not emit CPL. Panel **a** is reproduced with permission from REF.[79], AIP. Panel **b** is reproduced with permission from REF.[80], ACS. Panel **d** is reproduced with permission from REF.[118], ACS. Panel **e** is reproduced with permission from REF.[81], Wiley-VCH.

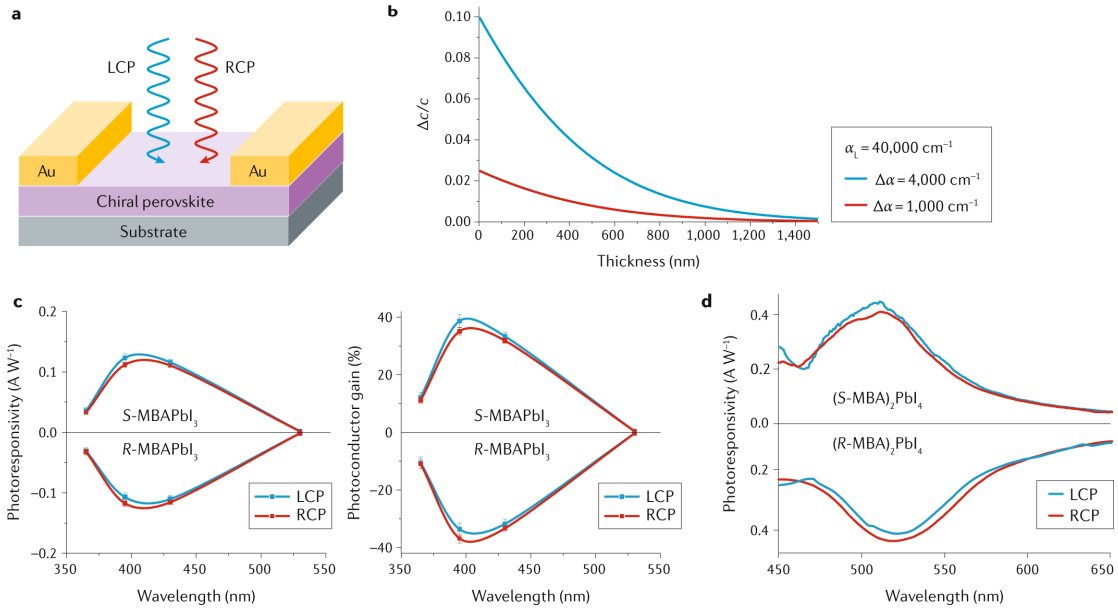

Fig. 6 | **Circularly polarized photodetectors based on chiral hybrid organic–inorganic perovskites. a** | Structure of a circularly polarized photodetector based on 1D chiral perovskites. **b** | The relationship between the thickness of the chiral medium and the ability to distinguish left-handed and right-handed circularly polarized light ($\Delta c/c$) for photoconductive circularly polarized light detection. Here assume the absorption coefficients of LCP (α_L) for chiral medium is 4000 cm^{-1}, a larger absorption difference ($\Delta\alpha$) between LCP and RCP light could give higher distinguishability (blue line, $\Delta\alpha$=4000 cm^{-1} vs. red line, $\Delta\alpha$=1000 cm^{-1}). **c** | The photoresponsivity and photoconductor gains of the 1D chiral perovskite-based circularly polarized photodetectors under left-handed and right-handed circularly polarized light, LCP and RCP light respectively. *R*-MBAPbI$_3$ based photodetectors exhibit larger RCP photoresponsivity and photoconductor gains than LCP, while the reverse was observed for *S*-MBAPbI$_3$. **d** | The photoresponsivity of a 2D chiral perovskite-based circularly polarized photodetector under LCP and RCP light. A similar trend was also observed for (*R*-MBA)$_2$PbI$_4$ and (*S*-MBA)$_2$PbI$_4$. Panels **a, b** and **c** are reproduced with permission

from REF.[38], Springer Nature. Panel **d** is reproduced with permission from REF.[39], ACS.

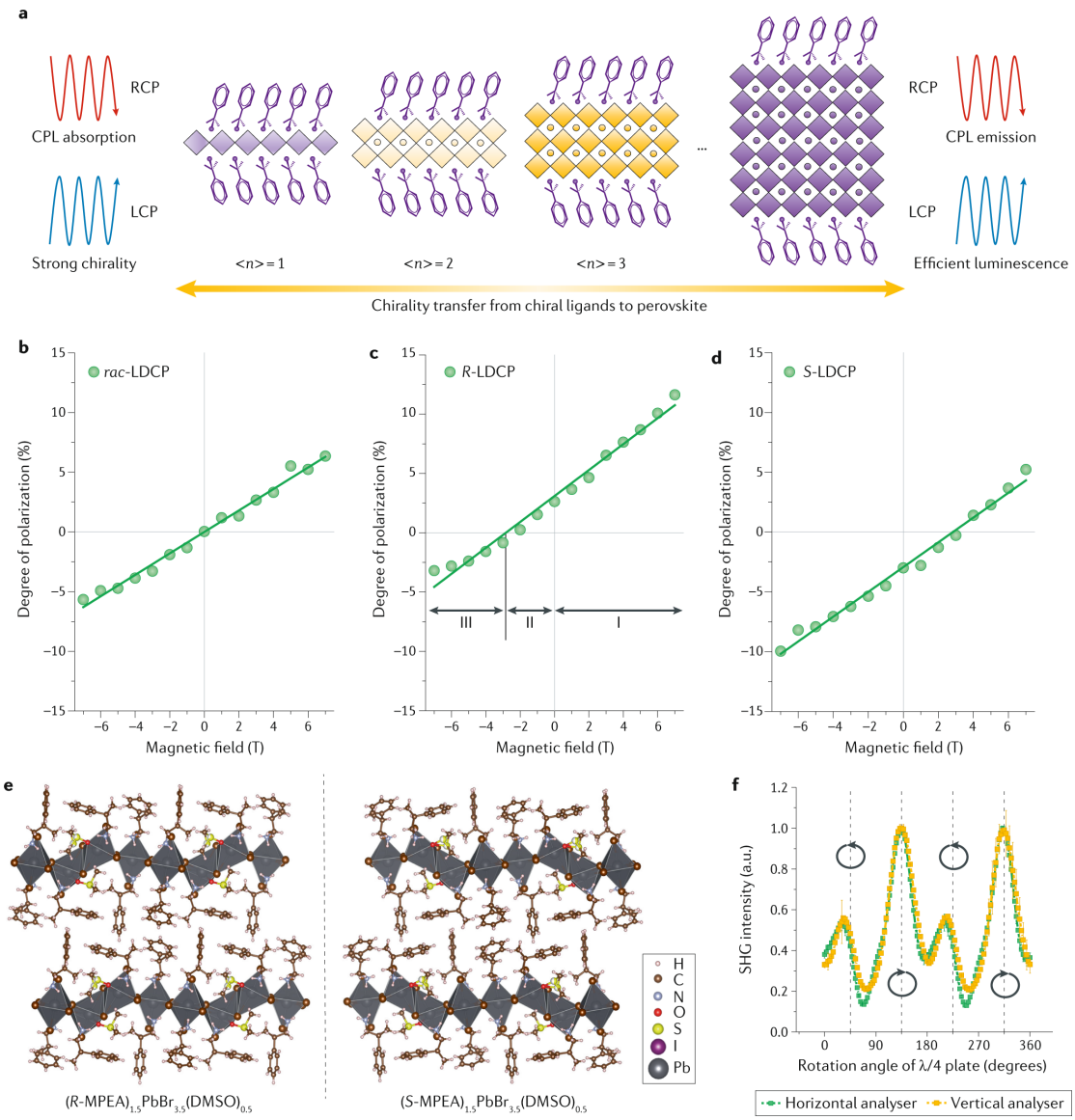

Fig. 7 | **Spin manipulation and nonlinear chiroptical effects in chiral perovskites.** **a** | Schematic illustration of the structures of low-dimensional chiral perovskites (LDCPs) with different numbers of inorganic layers (<n>). Smaller <n> could give strong chirality owing to the large mole fraction of chiral ligands, while larger <n> could give strong photoluminescence through energy funneling. Thus, there is a balance between strong chirality and high PLQY for LDCP. The degree of photoluminescence

polarization for *rac*-LDCP (panel **b**), *R*-LDCP (panel **c**) and *S*-LDCP (panel **d**) as a function of magnetic field is also shown and fitted by Equation 3 (green line). **e** | The crystal structures of $(R\text{-MPEA})_{1.5}PbBr_{3.5}(DMSO)_{0.5}$ and its enantiomer $(S\text{-MPEA})_{1.5}PbBr_{3.5}(DMSO)_{0.5}$. **f** | Polarization-dependent second-harmonic generation (SHG) for $(R\text{-MPEA})_{1.5}PbBr_{3.5}(DMSO)_{0.5}$ nanowires. Through rotating the λ/4 wave plate, the excitation can be modulated from linear polarization to circular polarization (the circular arrows refer to left and right circular polarization). The excitation wavelength is 850 nm and the detection wavelength is 425 nm. Vertical (yellow line) and horizontal analyzer (green line) is used to analyze the polarization of the generated SHG signal. Panels **a**, **b**, **c** and **d** are reproduced with permission from REF.[83], Springer Nature Limited. Panels **e** and **f** is reproduced with permission from REF.[48], ACS.

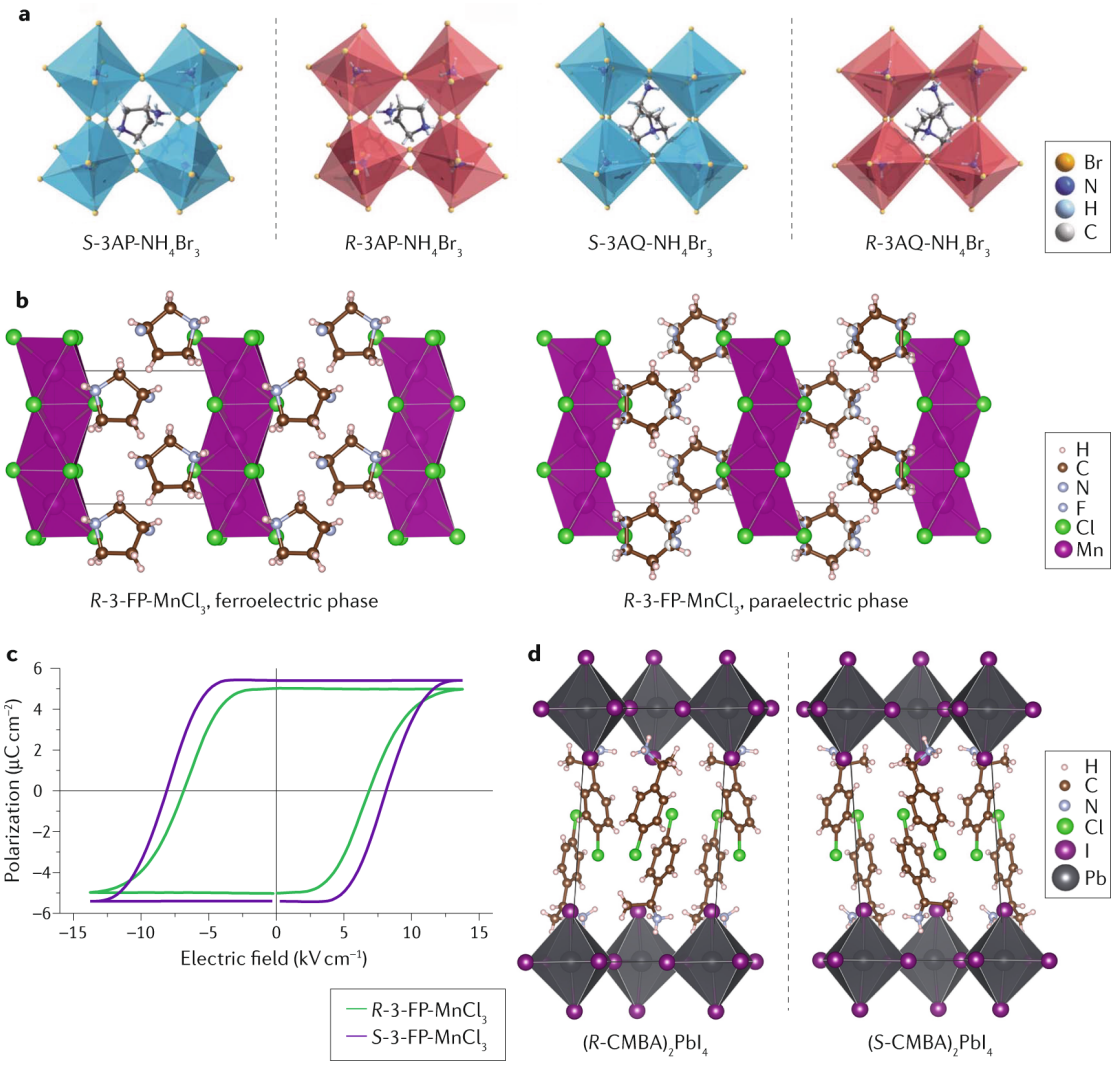

Fig. 8 | **Chiral perovskite-based ferroelectrics**. **a** | The crystal structures of *S*-3AP-NH_4Br_3 and its enantiomer *R*-3AP-NH_4Br_3 (left) and of *S*-3AQ-NH_4Br_3 and its enantiomer *R*-3AQ-NH_4Br_3 (right) in the ferroelectric phase (space group $P2_1$, transition temperature 293 K). **b** | The crystal structures of *R*-3-FP-$MnCl_3$ in the ferroelectric phase (space group $P2_1$, transition temperature 298 K, left) and in the paraelectric phase (space group $C222_1$, transition temperature 363 K, right). **c** | Ferroelectric hysteresis loops of *R*-3-FP-$MnCl_3$ (green) and *S*-3-FP-$MnCl_3$ (blue) single crystals; measurements were performed along the polar *b* axis at 313 K. **d** | The crystal structures of (*R*-CMBA)$_2PbI_4$ and its enantiomer (*S*-CMBA)$_2PbI_4$ in the ferroelectric phase (space group *P*1, transition temperature 293 K). Panel **a** is reproduced with

permission from REF.[84], AAAS. Panels **b** and **c** are reproduced with permission from REF.[41], ACS. Panel **d** is reproduced with permission from REF.[40], Wiley-VCH.

BOX 1 | Key terms

[H3] Sohncke space groups. The Sohncke space groups are the 3D space groups containing only operations of the first kind (rotations, roto-translations, translations). Among the 230 types of space groups, 65 are Sohncke (FIG. 3a)[91,95]. If a material's crystal structure belongs to a Sohncke space group, that material is chiral.

[H3] Neumann–Curie principle. The Neumann–Curie principle defines the relationship between Sohncke space groups and the corresponding properties, such as circular dichroism, second harmonic generation (SHG) and ferroelectricity (FIG. 3b)[89,90]. For instance, all chiral single crystals exhibit optical rotation and circular dichroism. However, optical rotation and circular dichroism can also be observed in non-centrosymmetric achiral point groups such as S_4, C_s, C_{2v} and D_{2d}. Similarly, most of the Sohncke groups are SHG active, but not those in the point groups O, D_4 and D_6.

[H3] Circular dichroism. Circular dichroism is a phenomenon whereby a material absorbs more of one circular polarization than the other, making the transmitted light elliptical (FIG. 3c)[46]. The degree of chirality can be represented in terms of ellipticity (θ, in mdeg)[97] or anisotropy factor (g_{abs})[98].

[H3] Ellipticity. The ellipticity (θ, in mdeg) is calculated based on the equation:

$$\theta\ (mdeg) = \Delta A \left(\frac{\ln 10}{4}\right)\left(\frac{180000}{\pi}\right) \qquad \textbf{(1)}$$

where ΔA is the difference in absorption of the left-handed (A_L) vs. right-handed circularly polarized light (A_R)

[H3] Anisotropy factor. The anisotropy factor[98] is the ratio of circular dichroism to conventional absorption, defined by:

$$g_{\mathrm{abs}} = \frac{A_L - A_R}{(A_L + A_R)/2} \qquad \textbf{(2)}$$

In this scale, the values range from -2 to 2 (absorbing only left-handed circularly polarized, LCP, or right-handed circularly polarized, RCP, light) to 0 (absorbing both equally).

[H3] Circularly-polarized photoluminescence (CPPL). CPPL results from different emission strengths of LCP vs. RCP light. The degree of photoluminescence polarization (DP) is given by:

$$DP = \frac{I_L - I_R}{I_L + I_R} \qquad \textbf{(3)}$$

where I_L and I_R are the emission intensities of LCP and RCP light, respectively. Values of DP close to -1 or 1 indicate pure RCP or LCP photoluminescence, whereas a value of 0 indicates no CPPL.

[H3] Cotton effect. The Cotton effect shifts absorption spectra for LCP vs. RCP light, resulting in the characteristic dispersive feature in circular dichroism spectroscopy.

[H3] Two-photon absorption-based upconverted photoluminescence (TP-UPL). TP-UPL occurs when a fluorophore absorbs two photons whose combined energy equals that of the electronic transition. Fluorescence resulting from this process occurs at a higher energy than that of the incoming photons (upconverted fluorescence, FIG. 3d).

[H3] Second-harmonic generation. SHG, also called frequency doubling, is a nonlinear optical process in which two photons interact with a nonlinear material to effectively combine to form new photons with twice the frequency of the initial photons (FIG. 3e)[99].

[H3] Ferroelectricity. Ferroelectric materials have intrinsic spontaneous electric polarization, even in the absence of an applied electric field (FIG. 3f). Ferroelectric materials are described using the saturated polarization[100] and coercivity[88]. The saturated polarization is the largest ferroelectric polarization that the material achieves under an external electric field, whereas coercivity is the minimum electric field required to depolarize a ferroelectric material after it has been driven to saturation.